Remote Sensing of Environment 345 (2026) 115602



Contents lists available at ScienceDirect

Remote Sensing of Environment

journal homepage: www.elsevier.com/locate/rse





LAPAC: A self-adaptive atmospheric correction method for fine-resolution satellite imagery using pseudo-invariant features from Landsat archive

Wenchang Li, Tao He *

Hubei Key Laboratory of Quantitative Remote Sensing of Land and Atmosphere, School of Remote Sensing and Information Engineering, Wuhan University, Wuhan 430079, China

ARTICLE INFO

Editor: Jing M. Chen

Keywords:
Atmospheric correction
Landsat
Surface reflectance
Pseudo-invariant features

ABSTRACT

Atmospheric correction is essential to ensure accurate land-surface applications of satellite data. Existing physics-based methods for fine-spatial-resolution sensors primarily rely on concurrent and accurate atmospheric parameters, which are usually difficult to obtain without the help of external resources and may lead to processing delays. This study proposes the LAPAC (Landsat Archive–based Pseudo-invariant Feature Atmospheric Correction) algorithm, a near-real-time method for retrieving surface reflectance without external atmospheric inputs. LAPAC extracts pseudo-invariant features (PIFs) from the long-term U.S. Geological Survey (USGS) Landsat surface reflectance archive and combines their historical reflectance stability with precomputed radiative transfer simulations to constrain a self-adaptive, pixel-wise inversion of surface and atmospheric parameters. Unlike methods limited to dark or bright targets, LAPAC is applicable across diverse surface conditions. Evaluations against USGS products under various aerosol optical depth and land-cover conditions showed strong agreement across all bands, with a mean coefficient of determination (R^2) of 0.91, $|\text{bias}| \leq 0.015$, and root-mean-square errors (RMSEs) generally below 0.016. Validation against ground measurements at four sites further demonstrated strong accuracy, with R^2 values ranging from 0.832 to 0.985 and RMSEs from 0.014 to 0.030. In addition, PIFs derived from Landsat 8 were transferable to Landsat 7, improving cross-sensor consistency and reducing the overall bias relative to Landsat 8 from 0.006 for the USGS products to 0.002. Overall, LAPAC allows for accurate and timely surface reflectance retrieval from Landsat imagery without concurrent external atmospheric inputs, as well as enabling consistent mapping of long-term surface reflectance across different Landsat sensors.

1. Introduction

In optical satellite remote sensing, the radiance measured by a satellite sensor is determined not only by the surface reflectivity but also by atmospheric effects, including aerosol scattering, molecular scattering, and absorption (Coleman et al., 2024). Atmospheric correction is necessary to retrieve accurate surface reflectance by removing the impact of atmospheric effects (Roy et al., 2014; Wang et al., 2016). In quantitative remote sensing applications, surface reflectance is a fundamental input for the derivation of higher-level surface geophysical parameters such as leaf area index (Jin et al., 2019), soil moisture content (Zhang et al., 2022) and land surface temperature (Cheng et al., 2021), as well as for retrieving atmospheric properties (Chen et al., 2024; Li et al., 2023).

The Landsat program represents a key milestone in the transition from coarse- to fine-spatial resolution Earth observation and serves as a foundation for atmospheric correction research and surface reflectance product generation (Claverie et al., 2018; Flood, 2017). In this study, fine-spatial-resolution optical imagery refers to data with spatial resolutions of 10–50 m, including the 30-m Landsat observations examined here. Surface reflectance products for Landsat 4 TM, Landsat 5 TM, and Landsat 7 ETM+ Collection 2 data were generated using the Landsat Ecosystem Disturbance Adaptive Processing System (LEDAPS) (Masek et al., 2012, 2013), while reflectance products for Landsat 8 OLI and Landsat 9 OLI Collection 2 were produced using the Land Surface Reflectance Code (LaSRC) (Vermote et al., 2016). Both algorithms are physics-based, using radiative-transfer simulations, look-up tables, and ancillary atmospheric information such as ozone, water vapor, and surface pressure.

Traditional physics-based atmospheric correction requires

* Corresponding author.
E-mail address: taohers@whu.edu.cn (T. He).

https://doi.org/10.1016/j.rse.2026.115602
Received 6 April 2026; Received in revised form 23 July 2026; Accepted 28 July 2026
Available online 10 August 2026
0034-4257/© 2026 Elsevier Inc. All rights are reserved, including those for text and data mining, AI training, and similar technologies.

comprehensive and accurate atmospheric parameters, relying either on frequent, high-quality meteorological inputs or on highly accurate retrievals based on the imagery itself (Doxani et al., 2023; Nazeer et al., 2021). Aerosol optical depth (AOD), which represents the column-integrated extinction by aerosols, is a key parameter controlling aerosol-induced atmospheric effects. The dense dark vegetation (DDV) method retrieves AOD by identifying densely vegetated or other dark targets with low visible-band surface reflectance. The relatively aerosol-insensitive short-wave infrared (SWIR) reflectance near 2.1 μm is used to constrain the expected visible-band surface reflectance. The residual difference between observed and modeled TOA reflectance can then be attributed mainly to aerosols (Kaufman and Remer, 1994). LEDAPS applies the DDV method to retrieve AOD for each individual Landsat scene (Masek et al., 2006). Its applicability is limited where sufficient dark targets are absent, such as bright, urban, or arid surfaces. The Deep Blue (DB) algorithm complements DDV by using prior blue-band surface reflectance to retrieve AOD over bright surfaces (Hsu et al., 2004, 2006). However, static surface-reflectance priors can be unreliable over vegetated regions with substantial seasonal or interannual change (Hsu et al., 2013).

To address this limitation, LaSRC instead uses a global, temporally dynamic prior database derived from Moderate Resolution Imaging Spectroradiometer (MODIS) and Multi-angle Imaging Spectroradiometer (MISR) observations. The database relates red-to-blue reflectance ratios to the enhanced vegetation index and supports iterative pixel-level AOD retrieval across locations and times (Vermote et al., 2016). Water vapor, another highly dynamic constituent of the Earth's atmosphere (Neelin et al., 2022), is commonly retrieved from remote sensing observations by exploiting the relationship between its amount and radiance ratios computed from absorption bands and non-absorption bands (Schläpfer et al., 1998). However, Landsat lacks dedicated spectral bands that can reliably support water-vapor estimation from the imagery alone (Frantz et al., 2019).

Beyond the target limitations of DDV and DB, physics-based correction depends on complete and temporally concurrent atmospheric inputs. This dependence can introduce processing delays and propagate auxiliary-data errors into surface-reflectance retrievals (Groeneveld and Ruggles, 2023). According to the USGS Collection 2 generation timeline, Level-2 products are typically available within approximately three days of Landsat 9 acquisition and four to eleven days of Landsat 8 acquisition. Moreover, LEDAPS and LaSRC use different auxiliary datasets and aerosol-retrieval strategies, potentially introducing sensor-dependent correction residuals and reducing long-term cross-sensor consistency (Che et al., 2021).

Precise measurement or estimation of each variable atmospheric constituent is only one route to decouple the atmospheric and surface signals captured by the sensors (Tanre et al., 1979). Alternatively, previous studies have established direct relationships between TOA reflectance (or radiance spectra) over stable surfaces and known surface reflectance (or typical land cover spectra) (Ientilucci and Adler-Golden, 2019; Yu et al., 2016). Such stable surfaces are commonly termed pseudo-invariant features (PIFs): pixels whose surface reflectance has sufficiently low and quantifiable temporal variability to constrain the surface contribution to the observed TOA signal. Image-based approaches typically treat atmospheric effects as an integrated correction factor to reduce reliance on timely and accurate estimates of multiple dynamic atmospheric parameters (Lhissou et al., 2020). Nevertheless, despite their operational advantages, existing image-based approaches generally exhibit lower accuracy than physics-based methods, a key limitation that this study aims to address (Nazeer et al., 2021).

When the concept of PIFs was first introduced, it was anchored to specific land-cover types, particularly artificial materials such as concrete, asphalt, and rooftops (Schott et al., 1988). More recently, several automatic techniques have been proposed for PIF extraction (Denaro and Lin, 2020; Syariz et al., 2019; Xu et al., 2021). However, most existing methods identify PIFs from an image pair and use them as tie points for relative normalization between a target and a reference image. Such pairwise strategies depend on reference-image quality and may produce inconsistent results when extended to long image series (Hall et al., 1991; Lin et al., 2019). Moreover, an individual image pair cannot establish an absolute reflectance reference or quantify the long-term stability of selected PIFs (Pons et al., 2014). After PIF selection, conventional normalization is generally performed to reduce radiometric differences unrelated to actual surface changes and to place the target and reference images on a comparable radiometric basis. It typically applies linear or low-order empirical mappings within the same measurement domain, such as DN-to-DN or TOA-reflectance-to-TOA-reflectance transformations (Chen et al., 2023; Kim and Han, 2021; Zhou et al., 2016). Although suitable for relative image matching, these simplified mappings do not explicitly represent the nonlinear atmospheric radiative-transfer process linking TOA and surface reflectance, which is more rigorously described by physically based radiative-transfer models (Emde et al., 2016; Servera et al., 2021).

This study addresses these gaps by proposing LAPAC (Landsat Archive–based Pseudo-invariant Feature Atmospheric Correction), a hybrid approach that combines long-term Landsat archive information with physically based radiative-transfer simulations. In LAPAC, PIFs are adaptively identified using archive-derived stability information, without requiring land-cover classification or class-specific reflectance priors. Pseudo-invariant does not indicate perfectly unchanged surface reflectance, but rather reflectance with sufficiently small and quantifiable temporal variability to provide a reliable constraint on the surface component of the observed TOA signal. Rather than using PIFs merely to fit a scene-to-scene empirical normalization equation, LAPAC incorporates the adaptively generated, archive-constrained PIF reference into an iterative, pixel-wise inversion of surface and atmospheric parameters. The PIFs therefore act as physical constraints on the nonlinear TOA-to-surface-reflectance relationship represented by precomputed radiative-transfer simulations.

The scientific innovation of LAPAC lies in three advances: (1) atmospheric correction without concurrent external meteorological inputs; (2) applicability across diverse surface conditions rather than only dark or bright targets; and (3) improved consistency of long-term surface-reflectance records across Landsat sensors through transferable archive-based constraints. In this framework, the Landsat archive serves not only as a historical data resource, but also as a physically informative reference for self-adaptive atmospheric correction.

The remainder of this paper is organized as follows. Section 2 describes the LAPAC framework, including PIF extraction, construction of the historical reference, and iterative atmospheric-correction procedure. Section 3 presents validation results under varying atmospheric and land-cover conditions. Section 4 discusses the method's applicability, limitations, and cross-sensor consistency. Section 5 summarizes the main conclusions.

2. Methodology

2.1. Theoretical basis

The atmospheric correction method employed in this study is based on the inversion of a relatively simple equation under the Lambertian assumption and in the absence of adjacency effects (Vermote et al., 2016). This equation accounts for a simplified coupling between atmospheric gas absorption and scattering by molecules and aerosols, and is computed following Eq. (1) embedded in the 6S radiative transfer code (Vermote et al., 2006), which can be reformulated as Eq. (2):

$$\rho_{TOA} = \rho_{atm} + Tr_{atm}^{*} \frac{\rho_s}{1 - S_{atm}^{*} \rho_s}, \quad (1)$$

$$1\Big/\rho_s = \frac{1}{\frac{1}{Tr_{atm}}^{*}\rho_{TOA} - \frac{\rho_{atm}}{Tr_{atm}}} + S_{atm}, \tag{2}$$

where ρ_{TOA} represents the TOA reflectance, ρ_s the surface reflectance, Tr_{atm} the total atmospheric transmittance, S_{atm} the spherical albedo, and ρ_{atm} the intrinsic atmospheric signal. Further simplification leads to Eq. (3):

$$1\Big/\rho_s = \frac{1}{xa^{*}\rho_{TOA} - xb} + xc, \tag{3}$$

$$xa = \frac{1}{Tr_{atm}}, \tag{4}$$

$$xb = \frac{\rho_{atm}}{Tr_{atm}}, \tag{5}$$

$$xc = S_{atm}, \tag{6}$$

where Eq. (4), Eq. (5), and Eq. (6) represent the three atmospheric correction coefficients xa, xb, xc, each composed of physically meaningful quantities. Atmospheric correction coefficient inversion can be formulated as an optimization problem, where the objective is to find the optimal solution that minimizes the error function defined in Eq. (8).

$$\widehat{\rho}_s = \frac{1}{\frac{1}{xa\cdot\rho_{TOA} - xb} + xc}, \tag{7}$$

$$error = \sum \left(\widehat{\rho}_s - \rho_s^{ref}\right)^2, \tag{8}$$

ρ_{TOA} is the TOA reflectance from the target image to be processed, ρ_s^{ref} is the reference surface reflectance synthesized from historical satellite data (Section 2.2.1), and $\widehat{\rho}_s$ denotes the surface reflectance predicted for the target image. The sample pairs (ρ_{TOA}, ρ_s) are selected using PIFs, based on the long-term variation of surface reflectance (Section 2.2.1) and the differences between the TOA reflectance of the target image and the reference surface reflectance (Section 2.2.2). Furthermore, the initial values and boundary conditions required for the optimization model are obtained from the radiative transfer simulations (Section 2.2.3). In this way, the atmospheric correction coefficients for the samples are derived, and atmospheric correction is applied to the entire target image through post-processing.

2.2. Methodology framework

Based on the above principle, the atmospheric correction procedure adopted in this study consists of the following steps, as illustrated in Fig. 1. First, a reference image sequence is constructed for the target image, from which reference surface reflectance and land cover change information are extracted (Section 2.2.1). Second, based on the results of the first step and the TOA reflectance of the target image, PIF pixel sets are extracted (Section 2.2.2). Third, using radiative transfer simulation results, optimization model parameters are set automatically. The TOA reflectance of the PIF pixel sets and the synthesized reference surface reflectance from the first step are input to invert atmospheric correction coefficients. Finally, the derived atmospheric correction coefficients are applied in post-processing to perform atmospheric correction on the entire scene (Section 2.2.3).

2.2.1. Reference image sequence construction

To extract PIFs, a reference image sequence was constructed for each

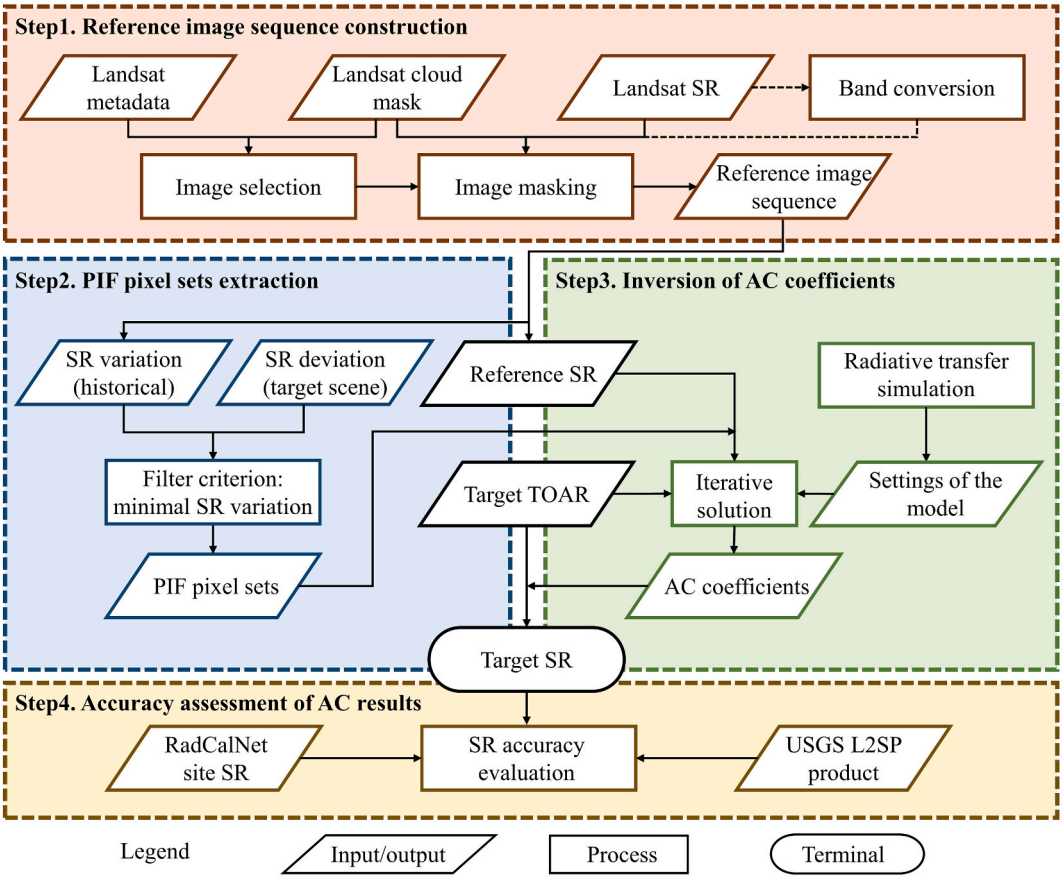


Fig. 1. Flowchart depicting atmospheric correction. The meaning of three different shapes is noted outside of the dashed line. The abbreviations that appear include: Surface Reflectance (SR), Top-of-Atmosphere Reflectance (TOAR), Atmospheric Correction (AC) and Pseudo-Invariant Feature (PIF).

target scene, consisting of two main steps: image selection and preprocessing. Image selection involves selecting candidate reference surface reflectance images based on the location and acquisition date of the target scene. Spatially, images covering the same spatial footprint as the target scene were selected. Temporally, images acquired within ±16 days of the target scene's day-of-year (DOY) from neighboring years were included. Only images with more than 30% valid pixel coverage (excluding clouds, cloud shadows, snow, and fill values) were retained. As the calculation of the standard deviation is required in subsequent steps, at least two valid observations are mathematically required. However, a larger number is preferable for characterizing temporal variability reliably. The initial neighboring-year search window was set to five years before and after the target year. If fewer than two valid observations remained after quality screening, the neighboring-year search window was expanded as needed. After cropping and cloud masking, the selected images formed a reference sequence, which, in addition to the two-dimensional spatial grids, included spectral bands and time dimensions, resulting in a four-dimensional matrix structure (Fig. 2).

The preprocessed reference image sequence was used to generate two key datasets: (1) reference surface reflectance images synthesized from the time series, and (2) quantitative indicators describing the temporal variation of surface reflectance. As discussed in Section 2.1, the reference surface reflectance images are required to provide values with broad spatial coverage (ensuring sufficient samples) and with acquisition dates close to that of the target image (ensuring value reliability). To mitigate the influence of abnormal reflectance values in the synthesis, we adopted the *Z*-score method to identify and exclude outliers. Outliers refer to individual pixel reflectance values in the historical image sequence that deviate substantially from the expected temporal distribution for that pixel. Such deviations may arise from residual cloud or cloud-shadow contamination, atmospheric-correction artefacts, or transient surface disturbances. Specifically, for each pixel and band, reflectance values with an absolute Z-score greater than 3 were treated as outliers and removed (Chikodili et al., 2021). Subsequently, the remaining valid surface reflectance values in the image sequence were combined using Gaussian-weighted averaging. The weights follow a Gaussian distribution with respect to temporal distance, assigning higher weights to observations closer in time to the target year. The reference surface reflectance at a given pixel was computed using the following formulae:

$$SR = \frac{\sum(\omega_i \cdot SR_i)}{\sum \omega_i}, \tag{9}$$

$$\omega_i = \exp\left(-\frac{\Delta t_i^2}{2\tau^2}\right), \tag{10}$$

where SR is the synthesized reference surface reflectance, SR_i is the surface reflectance value of the i-th image in the sequence, ω_i is the weight assigned to the i-th image, Δt_i is the absolute difference in years between the acquisition date of the i-th image and the target image and τ is a parameter controlling the rate of temporal weight decay. Smaller τ values emphasize recent data, while larger values emphasize long-term smoothing.

From the surface reflectance time series, not only absolute reflectance values but also reflectance variability are obtained. For each pixel, the CV is calculated from the time series to measure variability as follows:

$$CV = \frac{\sigma}{\mu}, \tag{11}$$

where σ represents the standard deviation, which measures the dispersion of data values, and μ is the mean value of the dataset. The CV is dimensionless. Larger values indicate greater relative variability, whereas smaller values indicate lower relative variability. Thus, it serves

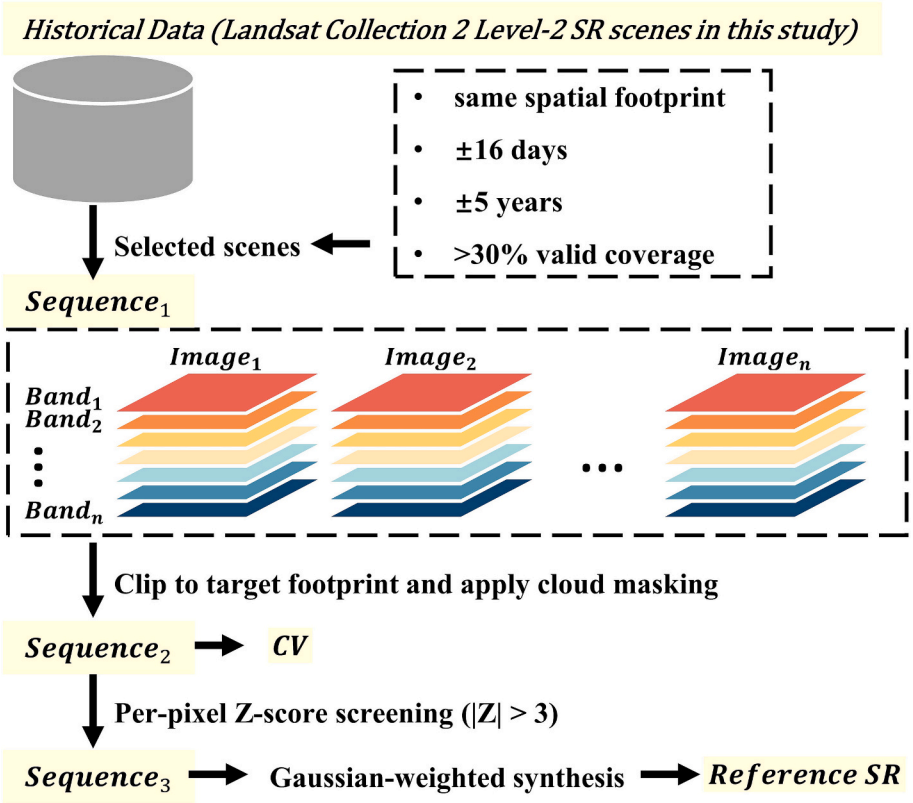


Fig. 2. Construction of the historical reference sequence and derivation of coefficient of variation (CV) and reference surface reflectance (SR). Historical data comprise selected Landsat Collection 2 Level-2 surface-reflectance scenes. Each image denotes one historical acquisition containing the corresponding spectral bands.

as an indicator of change across different land cover types. Notably, the *CV* is calculated using the original time series without excluding outliers, resulting in higher *CV* values at pixels with significant reflectance fluctuations. Such pixels are assigned lower priority in subsequent filtering steps.

Furthermore, the target and reference data used in this study may originate from different sensors. Spectral differences between corresponding bands of different sensors are primarily addressed by simulating surface reflectance and applying linear regression to derive band conversion coefficients (He et al., 2015, 2018). The datasets and methods employed are identical to those described in the cited references. The synthesized reference surface reflectance obtained from Eq. (9) is then converted into the target sensor's band-equivalent reflectance for subsequent processing.

2.2.2. PIF pixel sets extraction

A sufficient number of reflectance samples—i.e., TOA reflectance and surface reflectance pairs—are required for model inversion. In this study, we use Landsat images with a spatial resolution of 30 m. Pixels within a 100 × 100 window are grouped to form one sample set, resulting in a spatial resolution of 3 km for the derived AOD or atmospheric correction coefficients. This resolution is consistent with the MODIS 3 km DT AOD product and finer than the MODIS 10 km DT AOD, MODIS 10 km DB AOD, and VIIRS 6 km DB AOD products (Ettehadi Osgouei et al., 2022). However, not all pixels within a sample window are suitable for model input. Instead, only samples from PIFs that meet specific criteria are selected for input, as illustrated in Fig. 3.

We prioritize the pixel set with a smaller *CV*, in which the surface reflectance (Set 2 in Fig. 3) is more temporally stable, enabling the synthesized surface reflectance in Section 2.2.1 to be used as a reference for the surface reflectance on the target processing date. Additionally, cases must be considered in which surface reflectance appears stable over time (i.e., with a low *CV*) but undergoes changes on the target date—this is especially relevant when applying historical data to newly acquired imagery. However, the TOA reflectance from the target image cannot be directly compared with the synthesized surface reflectance because TOA reflectance includes atmospheric effects. Increased atmospheric aerosol can raise low reflectance through backscatter while reducing high reflectance through attenuation (Groeneveld et al., 2023). Previous studies have represented the atmospheric deviation between TOA and surface reflectance as a linear function of surface reflectance (Groeneveld and Ruggles, 2023). Specifically, the relationship can be written as:

$$TOAR - SR^{'} = m \cdot SR^{'} + b \tag{12}$$

The linearly normalized surface reflectance $SR^{'}$ is obtained as:

$$SR^{'} = \frac{TOAR - b}{m + 1}, \tag{13}$$

$$\Delta SR = |SR^{'} - SR|, \tag{14}$$

where *TOAR* is the TOA reflectance of the target image, $1/(m+1)$ and $b/(m+1)$ are the slope and intercept of the fitted linear model, respectively. $SR^{'}$ is the linearly normalized estimate of surface reflectance, *SR* is the synthesized reference surface reflectance from Section 2.2.1, and ΔSR is the absolute difference between the two. This preliminary normalization is used only to place the target-date TOA reflectance and synthesized surface reflectance in a comparable reflectance domain for change screening. Based on the low-*CV* pixel set (Set 2 in Fig. 3), pixels with smaller ΔSR are further selected to form Set 3 in Fig. 3. This ensures that the difference between TOA and surface reflectance used as model inputs is primarily due to atmospheric effects, minimizing the impact of land cover change on reflectance values for the target date.

2.2.3. Determination of atmospheric correction coefficients

As discussed in Section 2.1, inverting atmospheric correction coefficients requires not only a sufficient number of high-quality samples but also prior knowledge to set the relevant parameters of the

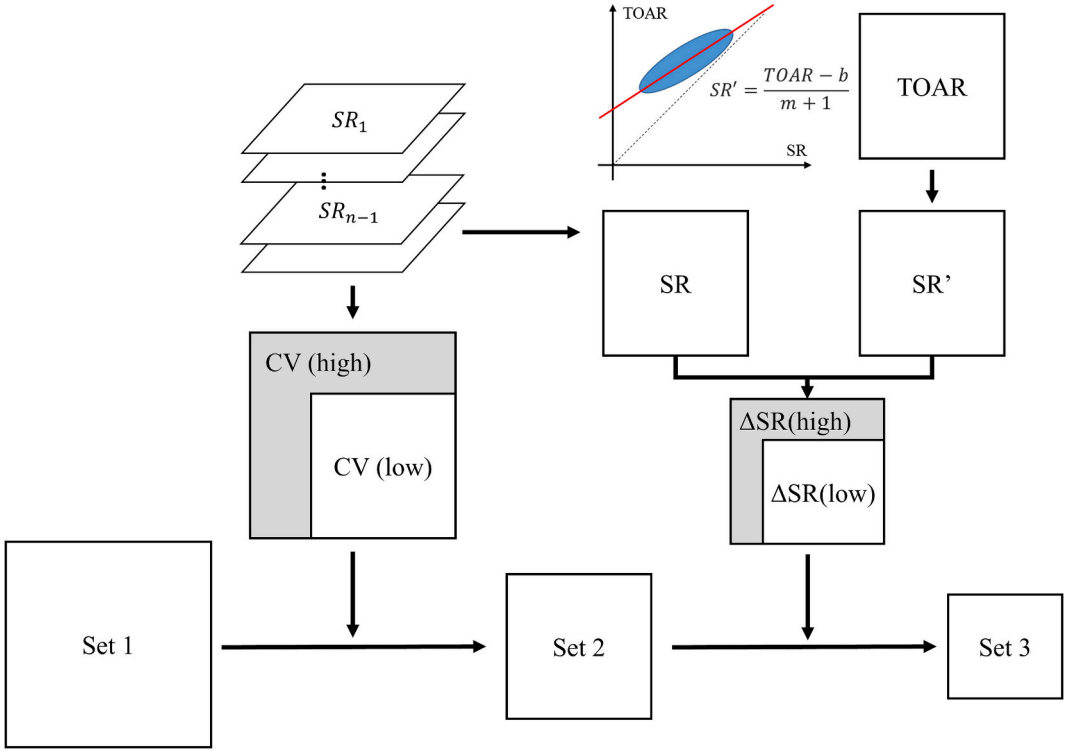


Fig. 3. Schematic diagram of the PIF pixel set extraction method. Set 1 is filtered by *CV* to obtain Set 2, which is then filtered by ΔSR to obtain Set 3. The abbreviations that appear include: Surface Reflectance (SR), Top-of-Atmosphere Reflectance (TOAR) and coefficient of variation (CV).

optimization model. We use the 6S radiative transfer model to simulate the variability of xa, xb, xc as functions of AOD, water vapor (WV), and ozone across spectral bands (Kotchenova et al., 2006; Kotchenova and Vermote, 2007). For each target scene, the 6S simulations were configured using the scene-specific observation geometry, location, and acquisition date, with the atmospheric profile and aerosol model selected according to latitude and season.

The simulations covered AOD values from 0.005 to 2.00, WV values from 0.005 to 8.00 g cm^{-2}, and ozone values from 0.005 to 0.5 atm-cm. These ranges were used to represent a broad sensitivity domain rather than to retrieve the actual AOD, WV, or ozone of the target scene. The resulting minimum and maximum values of xa, xb, xc were used as the lower and upper bounds of the optimization. Initial coefficient values were obtained from a nominal 6S simulation with AOD = 0.15 at 550 nm, WV = 2.0 g cm^{-2}, and ozone = 0.3 atm-cm. These values represent typical background atmospheric conditions and were used only to initialize the optimization. The final coefficients were determined by minimizing Eq. (8) within the 6S-derived bounds. Because the atmospheric correction coefficients vary significantly across spectral bands and therefore must be simulated independently.

Additional quality control constraints were imposed within each inversion sample set by requiring the coefficient of determination (R^2) in Eq. (15) to exceed a predefined threshold and the root-mean-square errors (RMSE) in Eq. (16) to fall below a specified limit. R^2 and RMSE quantify the agreement between the LAPAC-estimated surface reflectance and the corresponding archive-derived reference surface reflectance used in the inversion. Inversions failing either criterion were regarded as unreliable. Furthermore, the inversion results are categorized into three quality levels—high, medium, and low—based on whether the RMSE is less than or equal to 0.01, 0.02, or 0.05, respectively. This quality labeling, referred to as the ipflag, enables differentiated processing of results with varying internal inversion consistency in subsequent procedures. During PIF selection, the retained pixel percentage is adaptively reduced when the internal inversion RMSE exceeds 0.05, thereby excluding lower-quality samples and improving the consistency of the inversion set. A minimum retained proportion of 5% of the total valid pixels is maintained to ensure sufficient samples for iterative coefficient estimation. If the retained proportion reaches 5% and the internal inversion RMSE remains greater than 0.05, the tile is assigned a null value and its result is subsequently filled by spatial interpolation from neighboring valid tiles, rather than retaining an unreliable inversion solution.

$$R^2 = 1 - \frac{\sum_{i=1}^{n} (c_i - r_i)^2}{\sum_{i=1}^{n} (r_i - \bar{r})^2}, \tag{15}$$

$$\mathrm{RMSE} = \sqrt{\frac{1}{n} \sum_{i=1}^{n} (c_i - r_i)^2}, \tag{16}$$

It is generally assumed that AOD is spatially continuous, an assumption that has been employed in several studies for spatial interpolation of AOD (Chi et al., 2020; Yang and Hu, 2018; You et al., 2016). According to the radiative-transfer simulations, xa, xb, xc vary continuously with AOD, WV, and ozone. A set of atmospheric correction coefficients is derived through iterative optimization within a 3 km × 3 km tile. The tile size represents a practical compromise between resolving local atmospheric variation and retaining sufficient spatially distributed PIFs for a stable inversion. Smaller tiles may better capture sharp gradients near coastlines or local emission sources, but may contain insufficient PIFs to constrain the inversion reliably. Smoothing and interpolation are therefore applied to reduce discontinuities between adjacent valid tiles and to fill tiles where inversion fails. The post-processed atmospheric-correction coefficients, along with the TOA reflectance of each pixel, are substituted into Eq. (7) to calculate the corresponding surface reflectance, thus completing the atmospheric correction.

The LAPAC results were compared with official surface-reflectance products and independently evaluated against ground-based reference measurements. In addition to R^2 and RMSE, bias was defined in Eq. (17):

$$\mathrm{bias} = \frac{1}{n} \sum_{i=1}^{n} (c_i - r_i), \tag{17}$$

For all quantitative comparisons, r_i denotes the reflectance from the designated reference dataset, c_i denotes the corresponding reflectance from the dataset being evaluated or compared, $\bar{r}$ is the mean of the reference values, and n is the number of valid paired samples.

2.3. Data description

Landsat data were acquired from the USGS Earth Explorer portal (https://earthexplorer.usgs.gov/), including Level-1 products with systematic radiometric and geometric corrections, and Level-2 products with additional atmospheric correction (Crawford et al., 2023; Lubke et al., 2021; Rengarajan et al., 2020). Landsat scenes are organized using the Worldwide Reference System-2 (WRS-2), in which each scene is identified by a path/row combination that defines its geographic footprint. The Level-2 products serve not only as historical reference data for atmospheric correction, but also as a reference standard for cross-validation. The historical data used in Section 2.2.1 primarily comprises Landsat 8 surface reflectance from 2013 to the present. Contemporaneous Landsat 7 surface reflectance were also collected for the comparative experiment in Section 3.5. This study focuses on 30-m resolution imagery in the visible, near-infrared (NIR), and SWIR bands, including scenes from Landsat 7 ETM+ and Landsat 8 OLI sensors. In addition to scenes selected as examples listed in Table 1, additional images used for site-based validation are provided in Table 2.

To evaluate the robustness of LAPAC under different atmospheric conditions, three Landsat 8 OLI scenes acquired on 16 April 2015, 4 March 2017, and 13 April 2014 over WRS-2 path/row 123/032 were selected (Table 1). Atmospheric conditions were primarily characterized by AOD, derived from the MODIS/Terra+Aqua Land Aerosol Optical Depth Daily L2G Global 1 km SIN Grid product (MCD19A2), which provides 1 km spatial and daily temporal resolution (Lyapustin and Wang, 2022). The MCD19A2 product is publicly available at: https://ladsweb.modaps.eosdis.nasa.gov/search/order/1/MCD19A2–61. As shown in Fig. 4, AOD at 550 nm was extracted using quality-assured (QA) masks and averaged on a daily basis to obtain representative AOD values for each scene. The mean AOD values for areas corresponding to scenes 1, 2, and 3 are 0.09, 0.48, and 0.76, respectively.

To evaluate the robustness of LAPAC under different land-cover conditions, three Landsat 8 OLI scenes acquired on 26 August 2016 over path/row 121/025, 25 July 2016 over path/row 121/036, and 26 July 2016 over path/row 144/033 were selected (Table 1). Land cover

Table 1
Landsat Collection 2 Level-1 scenes to be atmospherically corrected.

Sensor	WRS-2 Path Row	Acquisition Time	Goal
Landsat 8 OLI	123/032	2015/4/16	Validation under different AOD
Landsat 8 OLI	123/032	2017/3/4	
Landsat 8 OLI	123/032	2014/4/13	
Landsat 8 OLI	121/025	2016/8/26	Validation under different land cover
Landsat 8 OLI	121/036	2016/7/25	
Landsat 8 OLI	144/033	2016/7/26	

Table 2
RadCalNet site measurements and corresponding Landsat imagery used in this study. "Number" indicates the number of coincident observations between ground and satellite data.

Site	Location	WRS-2 Path/ Row	Number (Landsat 8)	Number (Landsat 7)
RVUS	115.69°W, 38.50°N	040/033	112	61
LCFR	4.86°E, 43.56°N	196/030	60	21
GONA	15.12°E, 23.60°S	179/076	84	29
BSCN	109.62°E, 40.87°N	128/032	15	1

information was obtained from the first Landsat-derived annual China Land Cover Dataset (CLCD), which provides nationwide land cover and change dynamics across China from 1985 to 2023 at a spatial resolution of 30 m and a temporal resolution of one year (Yang and Huang, 2024). The CLCD dataset is publicly available at: https://zenodo.org/records/12779975. Clouds, cloud shadows, and snow present in individual scenes (shown as white areas in Fig. 5) were identified using the QA bands of the corresponding Landsat products (Foga et al., 2017).

In this study, in situ surface reflectance data from the Radiometric Calibration Network (RadCalNet) were used to assess the absolute accuracy of LAPAC (Bouvet et al., 2019). The data are publicly available at: https://www.radcalnet.org/. Currently, RadCalNet maintains five operational sites located in the United States (RVUS), France (LCFR), Namibia, and China (BSTN and BSCN). These sites acquire surface reflectance and atmospheric parameter measurements every 30 min between 09:00 and 15:00 local time. Surface reflectance is measured at 10 nm spectral intervals over the 400–2500 nm wavelength range, except for the Chinese sites, where the range is limited to 400–1000 nm. Among the Chinese sites, BTCN (an artificial target) exhibits greater measurement uncertainty than BSCN (a natural sandy surface) (Ma et al., 2020). Additionally, the target area at the BSTN site is only 48 m × 48 m (Li et al., 2015), meaning that a single 30 m Landsat pixel may contain multiple land cover types, potentially introducing significant reflectance errors. Therefore, data from the BSTN site were excluded from the analysis. After quality control (e.g., removing cloud-contaminated observations and requiring that the 1-km window around the site contain no pixels flagged as cloud or cloud shadow), matched in situ measurements and corresponding Landsat scenes were identified (Table 2). For Landsat 7, scenes were further retained only when the temporally closest Landsat 8 acquisition shared at least 70% overlap in common valid pixels within the jointly usable area. The analysis period spans from the beginning of data availability at each site through 2024 (Landsat 7 data were used only through 2021).

3. Results

3.1. Analysis of the reference image sequence and extracted PIF pixel sets

The Landsat 8 OLI scene acquired on 16 April 2015 over WRS-2 path/row 123/032 contains water bodies, urban areas, and vegetation with varying densities. This scene serves as an example to demonstrate the PIF pixel sets extraction results. The synthesized reference surface reflectance (denoted as "reference SR" in Fig. 6) contains 41,374,338 valid pixels, which is more than that of any individual image in the reference surface reflectance sequence. Moreover, the synthesized reflectance values are numerically closest to those of the temporally nearest image (acquired on 2015-05-02). Because *Z*-score filtering is applied to remove temporal outliers (as shown by the reduction in valid

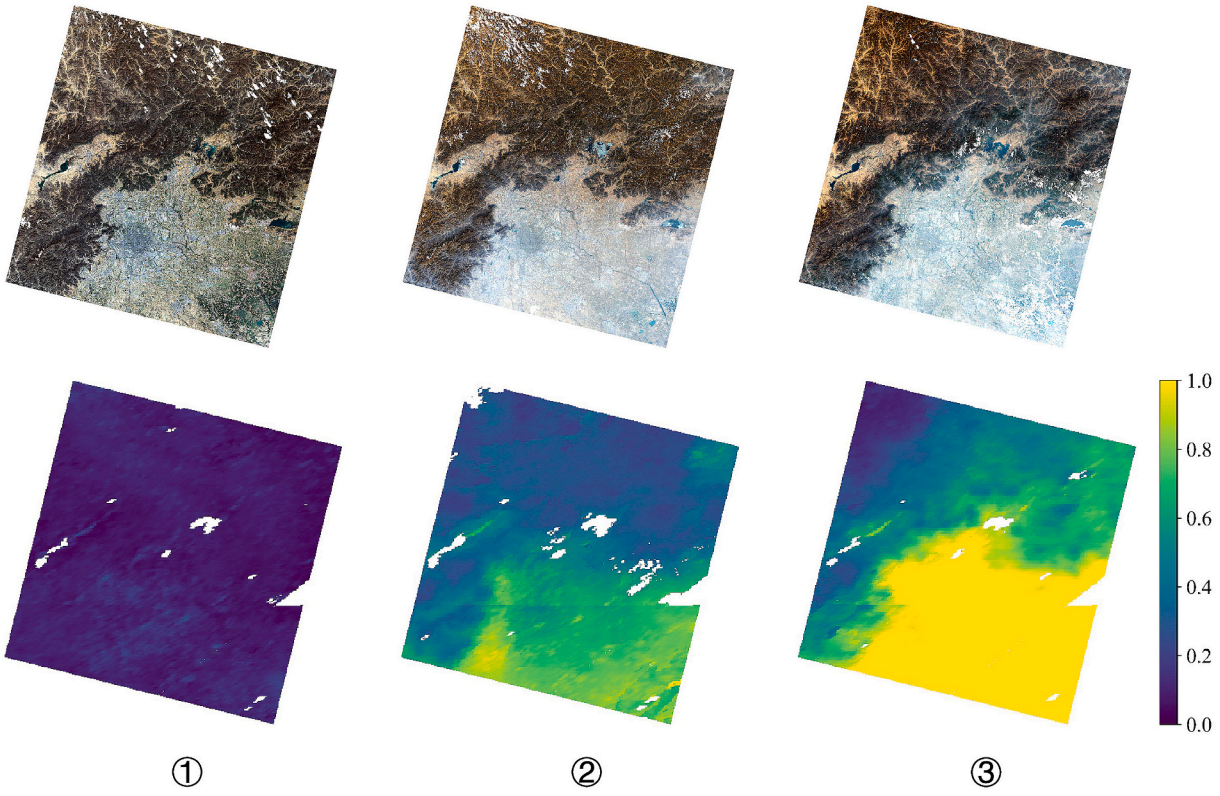


Fig. 4. RGB images of the Landsat 8 OLI scenes acquired on 16 April 2015, 4 March 2017, and 13 April 2014 over WRS-2 path/row 123/032, with corresponding AOD values shown below each image. The displayed images represent the full scenes. White regions indicate missing values in the MCD19A2 product. Each RGB image was stretched by excluding the 2nd and 98th percentiles of reflectance values for each band. All subsequent RGB visualizations were processed using the same method.

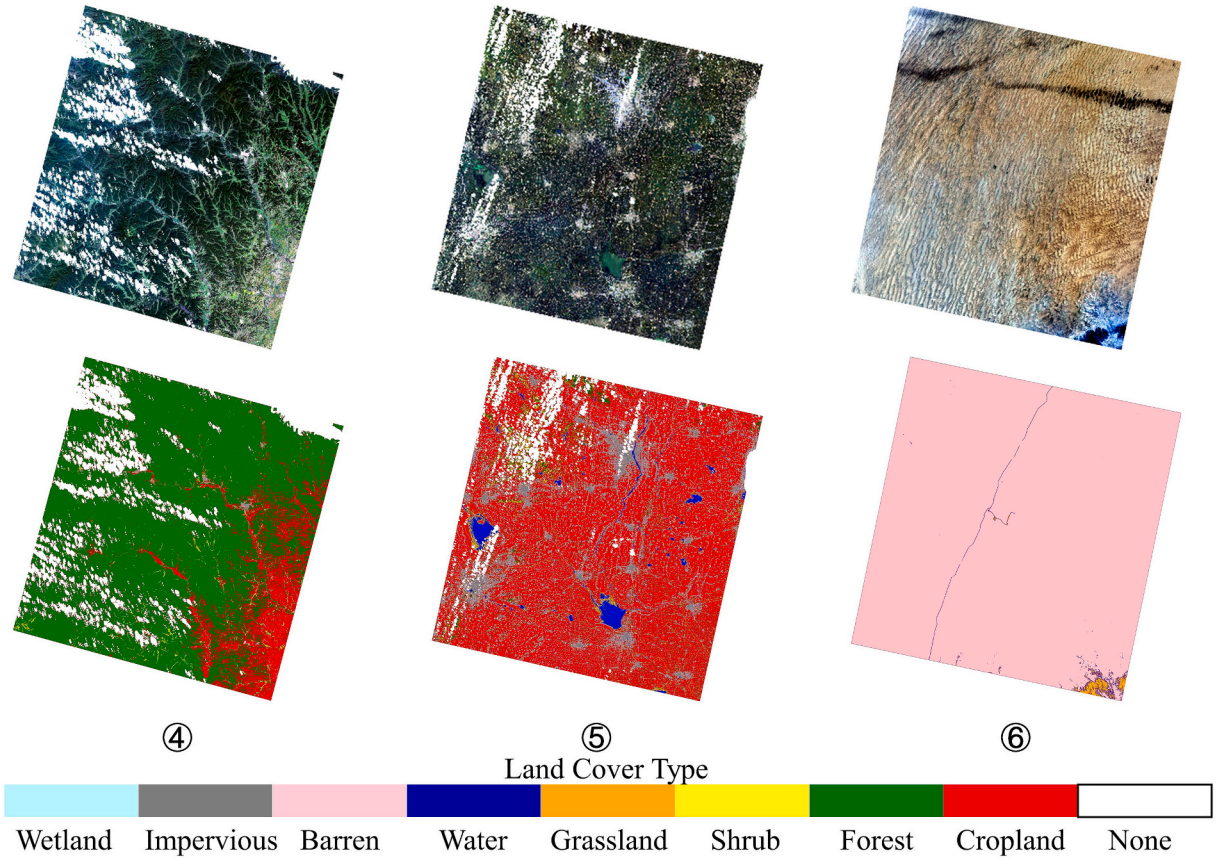


Fig. 5. RGB images of the Landsat 8 OLI scenes acquired on 26 August 2016, 25 July 2016, and 26 July 2016, with corresponding land cover conditions shown below each image. The displayed images represent the full scenes. White regions indicate clouds, cloud shadows, or snow as identified by the Landsat QA band.

values from N1 to N2 in the figure), the resulting dataset provides more abundant and accurate sample points for the subsequent inversion of atmospheric correction coefficients.

Fig. 7 shows the progressive reduction of candidate pixels within the selected 100 × 100-pixel subset. After *CV* screening, the retained pixels (Set 2; Fig. 7b) are concentrated in portions of the scene with low historical reflectance variability, whereas large areas of water and cropland are removed in this example. The remaining pixels are not restricted to a single land-cover type. Some agricultural-field pixels are retained because their historical reflectance variability is low within the reference period.The subsequent *ΔSR* screening further reduces Set 2 to the final PIF set (Set 3; Fig. 7c). Comparison with Fig. 7e shows that pixels with relatively large differences between the normalized target-image reflectance and the synthesized reference reflectance are preferentially excluded. Thus, the final PIFs represent pixels that satisfy both low long-term variability and consistency with the target-date reference condition. The retained land-cover composition is specific to this scene and should not be interpreted as indicating that any land-cover class is inherently stable or unstable.

Fig. 8 compares the relative land-cover composition before and after band-specific PIF screening. "All" denotes the percentage of each land-cover class among all valid pixels before PIF screening (Set 1), whereas B1–B7 denote the percentages of each class among the final PIF samples retained independently for Bands 1–7 (Set 3). Because the PIF-selection procedure is applied independently to each band using CV- and *ΔSR*-based criteria, the land-cover composition of the retained PIF samples differs among bands. Land-cover labels were not used during PIF selection. Instead, candidate pixels were ranked according to their historical CV and target-date *ΔSR*, and the retained proportion was adaptively adjusted to balance sample quantity and inversion quality.

Accordingly, differences in the proportions of cropland, forest, grassland, impervious surfaces, water, and other classes between the initial valid-pixel set and the final band-specific PIF sets reflect the relative temporal spectral consistency of individual pixels in this scene. They should not be interpreted as evidence that a particular land-cover class is inherently stable or unstable. For example, the reduced retention of cropland or forest pixels in certain bands indicates that some pixels in these classes did not satisfy the selection criteria for that scene and band. Conversely, the retention of some impervious pixels indicates only that those individual pixels met the CV- and *ΔSR*-based criteria.

3.2. Improvement of atmospheric correction results using PIFs

As discussed in Section 2.1, inversion of the atmospheric-correction coefficients requires both sufficient high-quality samples and physically plausible parameter bounds. We used the 6S radiative-transfer model to simulate the responses of xa, xb, xc to AOD, WV, and ozone for Landsat 8 OLI Bands 1–7. Fig. 9 shows the responses of xa, xb, xc to AOD (a–c), WV (d–f), and ozone (g–i), respectively.

All three coefficients vary monotonically with AOD, but their absolute magnitudes are not directly comparable because they represent different terms in the atmospheric-correction equation. Increasing AOD reduces total atmospheric transmittance, thereby increasing xa. It also increases intrinsic atmospheric reflectance through enhanced aerosol scattering, resulting in a pronounced increase in xb. By contrast, xc represents atmospheric spherical albedo and reflects the contribution of multiple scattering. The AOD-induced responses are generally stronger at shorter wavelengths because aerosol and molecular scattering decrease with wavelength.

In operational processing, LAPAC does not require scene-specific external WV or ozone inputs. Instead, the 6S simulations use the default atmospheric and aerosol configurations selected according to the

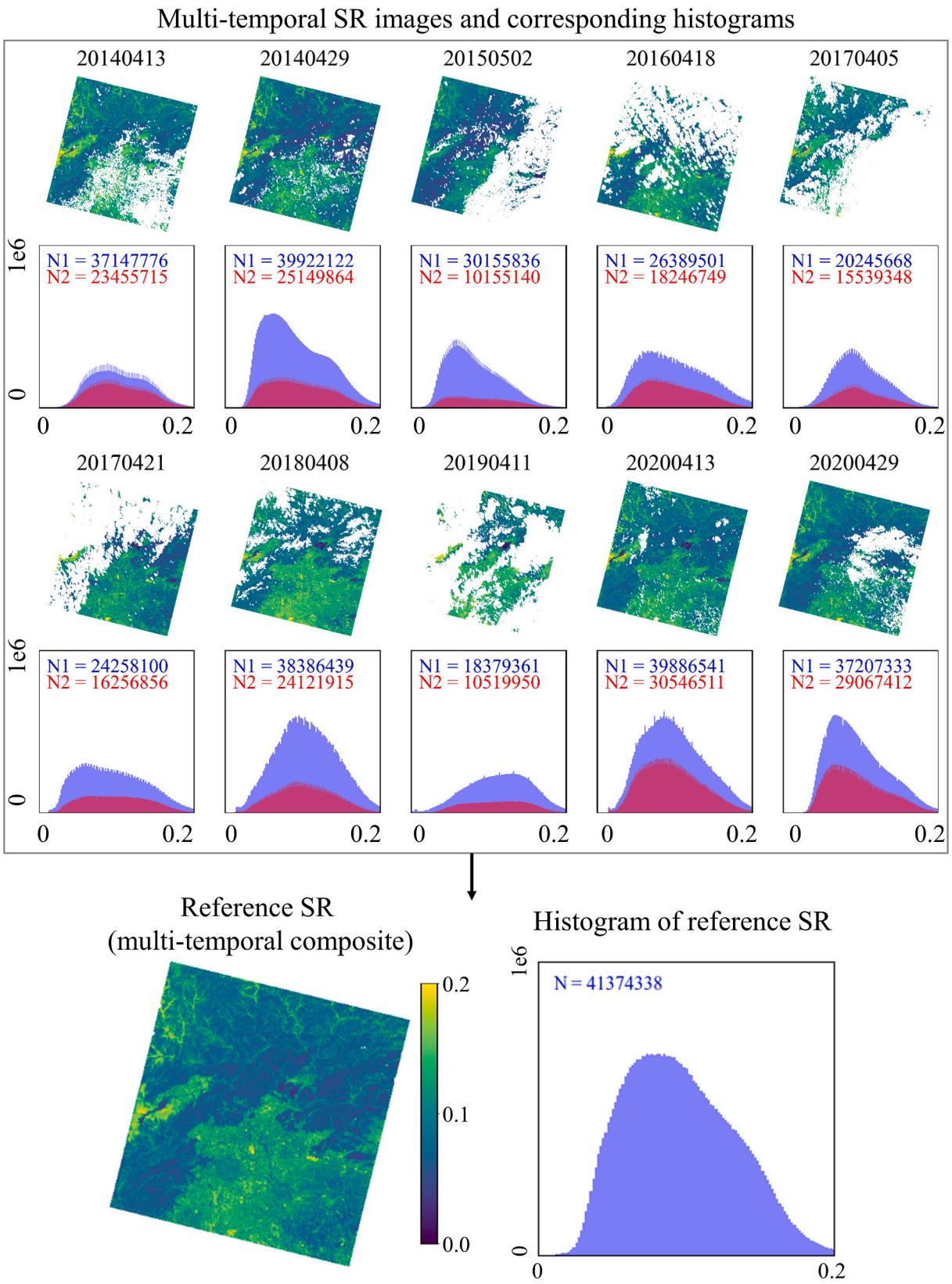


Fig. 6. Multi-temporal SR images in the red band and their corresponding histograms. White regions denote clouds, cloud shadows, background values, and other invalid pixels. For each histogram, blue and red colors represent the distributions before and after Z-score filtering, respectively. N1 and N2 denote the numbers of valid pixels before and after filtering. The reference SR is generated through multi-temporal compositing of the preprocessed SR images, and its corresponding histogram is shown on the right, where N denotes the number of valid pixels. (For interpretation of the references to colour in this figure legend, the reader is referred to the web version of this article.)

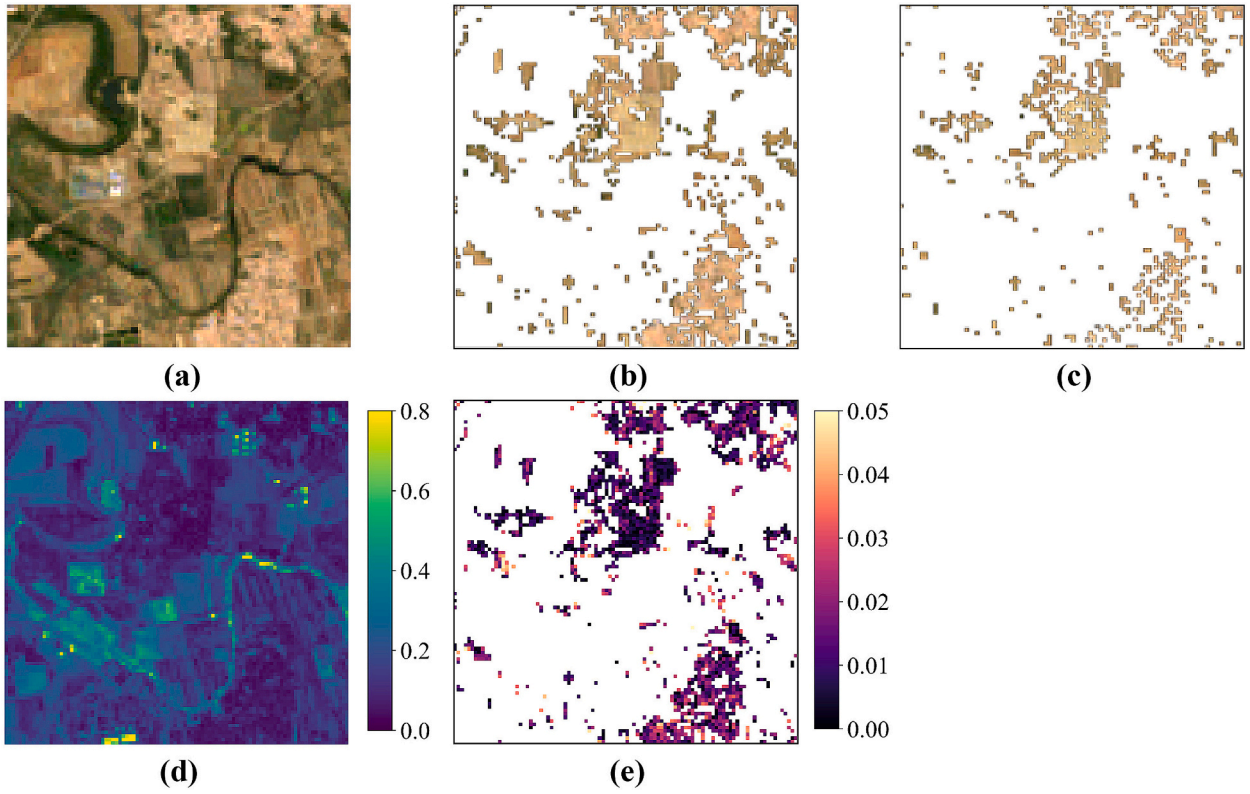


Fig. 7. Blue-band subset of the Landsat 8 OLI scene acquired on 16 April 2015 over WRS-2 path/row 123/032 (Band 2; rows 4800–4900; columns 4800–4900). (a) Initial candidate pixels (Set 1); (b) pixels retained after *CV* screening (Set 2); and (c) final PIFs retained after filtering by the absolute difference between the normalized target-image reflectance and the synthesized reference reflectance (ΔSR; Set 3). Panels (d) and (e) show the corresponding *CV* and ΔSR values, respectively. The black border indicates the boundary of the displayed image subset and has no analytical significance. (For interpretation of the references to colour in this figure legend, the reader is referred to the web version of this article.)

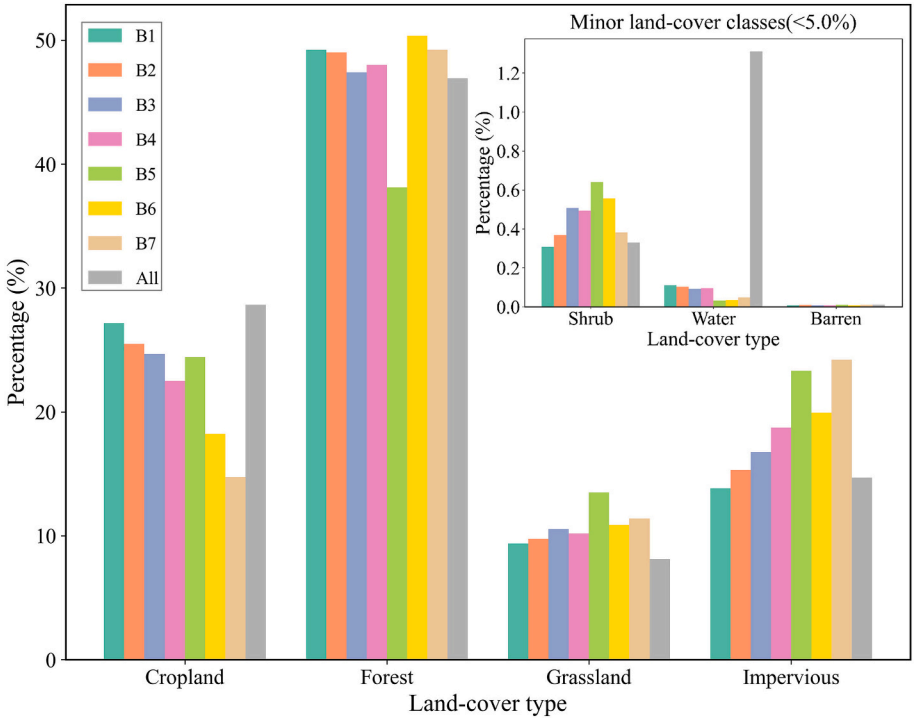


Fig. 8. Comparison of land-cover composition before and after band-specific PIF screening for the Landsat 8 OLI scene acquired on 16 April 2015 over WRS-2 path/row 123/032. "All" represents the percentage of each land-cover class among all valid pixels before PIF screening (Set 1). B1–B7 represent the percentages of each class among the final PIF samples retained independently for Landsat 8 OLI Bands 1–7 (Set 3). Classes with proportions below 5% are shown in the inset.

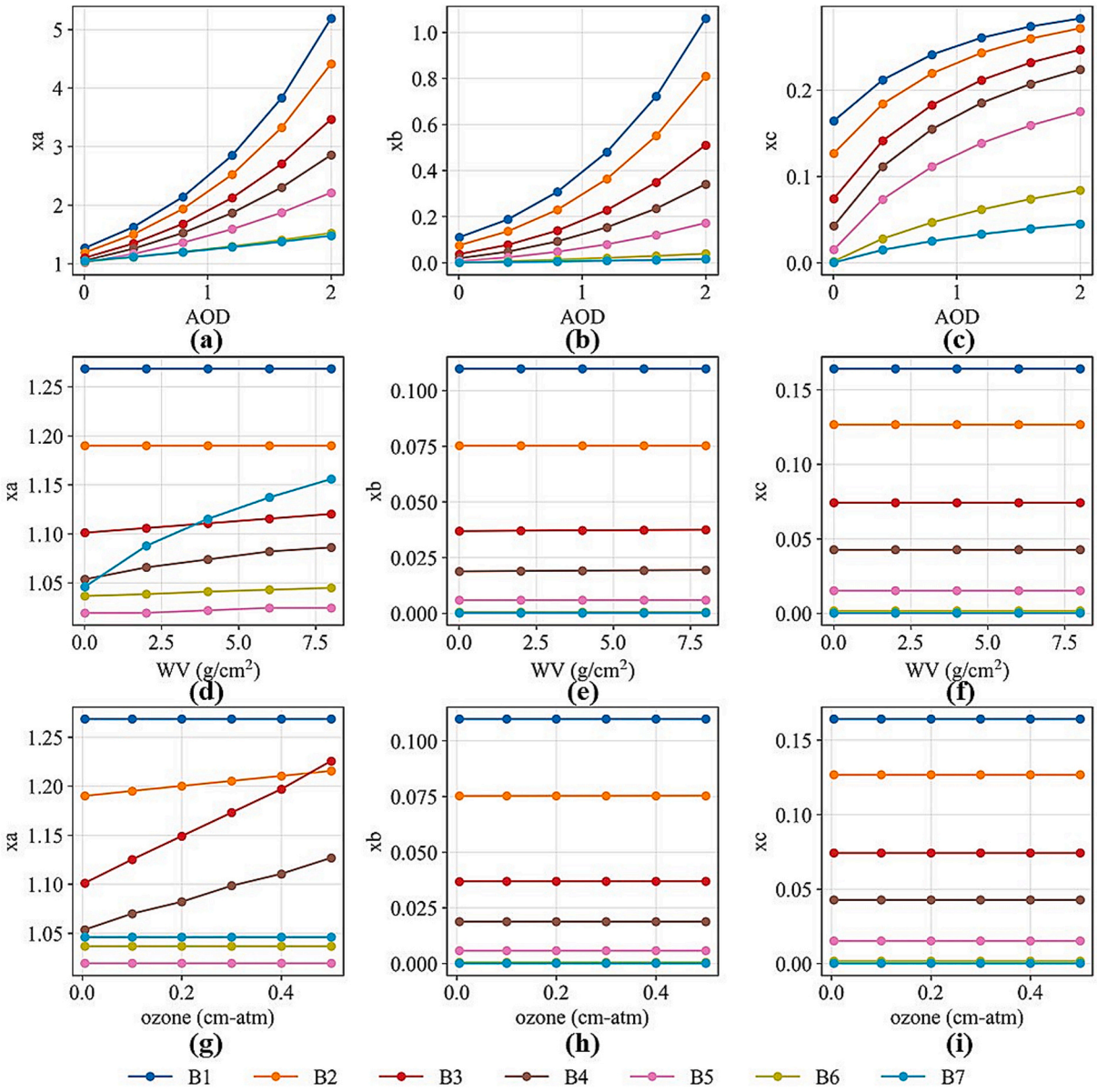


Fig. 9. Atmospheric-correction coefficients *xa*, *xb*, *xc* for Landsat 8 OLI Bands 1–7 as functions of (a–c) aerosol optical depth (AOD), (d–f) water vapor (WV), and (g–i) ozone. When one atmospheric parameter is varied, the other two are fixed at 0.005. The sampled values are AOD = 0.005, 0.40, 0.80, 1.20, 1.60, 2.00; WV = 0.005, 2.00, 4.00, 6.00, 8.00 g/cm^2; and ozone = 0.005, 0.1, 0.2, 0.3, 0.4, 0.5 cm-atm.

target latitude and season. This treatment does not neglect gaseous absorption, because its effects remain represented in the selected 6S atmospheric profile. The WV and ozone sensitivity analyses in Fig. 10d–i show that their effects are generally weaker than the AOD-induced variation in Fig. 10a–c and mainly affect *xa*, whereas *xb* and *xc* remain nearly constant over the simulated ranges. The responses are also monotonic, allowing the associated uncertainty to be incorporated into the coefficient bounds.

The most evident exception is *xa* for Band 7 under varying WV conditions. Band 7 is located in the SWIR region and remains sensitive to water-vapor absorption. Increasing WV reduces the band-integrated total atmospheric transmittance and consequently increases *xa*. This sensitivity is smaller than the AOD-induced variation but indicates a residual uncertainty for Band 7 when scene-specific WV is unavailable.

The TOA reflectance of the target image within the PIF pixel set extracted in Section 3.1, along with the synthesized reference surface reflectance, was used as inputs to the optimization model introduced in Section 2.1. The relationship between the two reflectance datasets is illustrated in Fig. 10(g). The atmospheric correction coefficients for each band are then applied to correct the TOA reflectance within the PIF pixel set. The comparison between the corrected surface reflectance and the reference reflectance is shown in Fig. 10(h). When the coefficients are applied to the entire tile, the resulting surface reflectance is compared with the LaSRC-corrected product in Fig. 10(i). To evaluate the effectiveness of PIF pixel set extraction, the above process is repeated using Set 1 (without PIF extraction) and Set 2 (using only CV-based extraction) as defined in Section 2.2.2. The reflectance from the sets is used as input to invert atmospheric correction coefficients. The corresponding correction results are shown in Fig. 10(a), (b), (c) and Fig. 10(d), (e), (f), respectively.

Fig. 10(a) shows the reflectance input to the model without any screening, resulting in larger bias and RMSE compared to Fig. 10(d) and Fig. 10(g), which makes the inversion of atmospheric correction coefficients more difficult. Although the error-minimizing inversion model can reduce bias to near zero, the RMSE in Fig. 10(b) remains relatively high due to the inclusion of many samples that remain inconsistent with

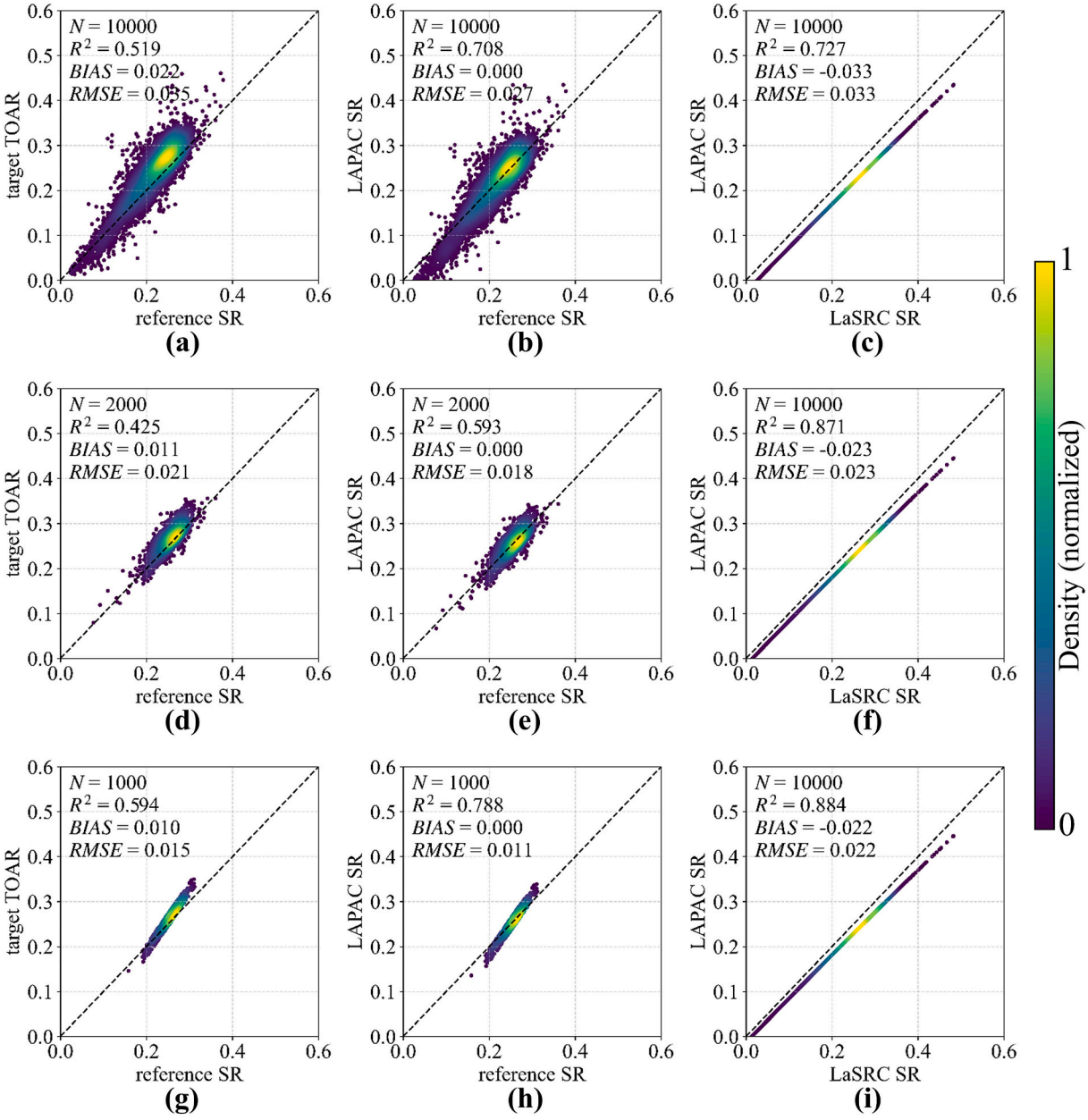


Fig. 10. Atmospheric-correction results for a SWIR-band subset of the Landsat 8 OLI scene acquired on 16 April 2015 over WRS-2 path/row 123/032 (Band 6; rows 4800–4900; columns 4800–4900). (a)(b)(c), (d)(e)(f), and (g)(h)(i) show the atmospheric correction results for Set 1, Set 2, and Set 3, respectively, as defined in Fig. 3. N indicates the number of valid values randomly selected from the study area. The density of the two-dimensional scatter points is estimated using Kernel Density Estimation (KDE) and normalized. The abbreviations that appear include: Surface Reflectance (SR), Top of Atmosphere Reflectance (TOAR).

the reference SR. Moreover, the PIF pixel set extraction not only statistically removes pixels with relatively large historical variability or target-date reference mismatch, facilitating the inversion, but also preserves temporally stable TOAR-SR pairs, resulting in more reliable correction coefficients.

The nearly linear relationships in the third column are expected because LaSRC and LAPAC both apply approximately linear transformations to the same target-scene TOA reflectance over the limited reflectance range of the tile. Therefore, both products preserve much of the spatial ordering of the original image, although their point clouds do not perfectly coincide with the 1:1 line, as indicated by the non-zero bias and RMSE values.

This conclusion is further supported by the spatial distribution of tile-level internal inversion RMSE across all bands of the full-scene image (Fig. 11). For each tile, RMSE was calculated between the LAPAC-estimated surface reflectance and the archive-derived reference surface reflectance for the samples used in the inversion. The resulting tile-level RMSE values were mapped to their corresponding spatial locations.

3.3. Validation of SR under various AOD and land cover

In Section 3.2, the atmospheric correction results for a single image slice were analyzed. However, for practical image processing, in order to avoid discontinuities between adjacent slices, the post-processing step described in Section 2.2.3 is required to obtain consistent scene-wide atmospheric correction coefficients and surface reflectance. To validate the accuracy of the surface reflectance derived from LAPAC under various atmospheric and land surface conditions, we utilized the AOD product and the land cover product from Section 2.3.

To evaluate the performance of the method under different AOD

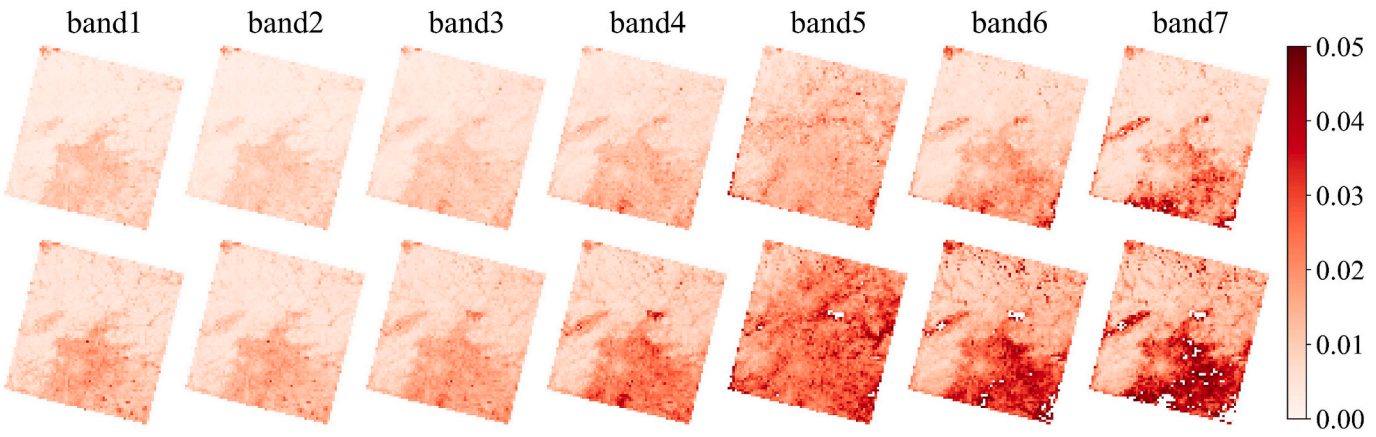


Fig. 11. Spatial distribution of internal inversion RMSE for Landsat 8 OLI Bands 1–7 over the full scene acquired on 16 April 2015. The first row shows tile-level RMSE obtained when the inversion was constrained using the final PIF set (Set 3), whereas the second row shows the corresponding RMSE obtained using all valid pixels without PIF screening (Set 1). RMSE was calculated between LAPAC-estimated surface reflectance and the archive-derived reference surface reflectance within each inversion tile.

conditions, we compared LAPAC-derived surface reflectance with the official LaSRC product. Fig. 12 summarizes R^2, bias, and RMSE for Bands 1–7 under low- (16 April 2015), medium- (4 March 2017), and high-AOD (13 April 2014) conditions. Overall, LAPAC shows consistently high agreement with LaSRC across all AOD levels. R^2 values are generally high, reaching 0.989 for Band 5 under low-AOD conditions and remaining above 0.5 for Band 1 under medium-AOD conditions, where the reflectance distribution is highly concentrated. The mean R^2 across all bands and AOD conditions is 0.91, demonstrating stable fitting performance across spectral and atmospheric variations. Bias is near zero across bands, with $|\text{bias}| \leq 0.015$, indicating limited systematic error. RMSE is likewise low, remaining $\leq$0.015 for all bands, which suggests controlled overall error. Notably, none of the three metrics exhibits an evident degradation trend under increasing AOD, suggesting that the reflectance estimation strategy based on pseudo-invariant features remains robust and applicable even under considerable aerosol variation.

Fig. 13 shows the RMSE distribution for LAPAC-derived surface reflectance relative to the LaSRC product across land-cover types. Overall, RMSE is low for most land-cover types, typically ranging from 0.004 to 0.016, indicating good agreement in most cases. However, performance varies by land-cover type. Barren land shows the lowest RMSE, remaining below 0.006 across all bands, indicating high consistency and stability. In contrast, forest, wetland, and grassland exhibit higher RMSE in the NIR (Band 5), reaching 0.028, 0.026, and 0.023, respectively. This pattern suggests larger uncertainties in NIR reflectance estimation over vegetated surfaces.

To examine whether LAPAC–LaSRC agreement varies across spectral bands and signal ranges, Fig. 14 compares the band-wise kernel density distributions of LAPAC and LaSRC surface reflectance. The two distributions overlap closely for Bands 1–7, indicating that LAPAC generally reproduces the reflectance distribution of the LaSRC product.

The paired-sample statistics shown in Fig. 14 further support this consistency. The R^2 values range from 0.912 to 0.994 across Bands 1–7, while bias ranges from −0.0019 to 0.0022. RMSE values range from 0.0081 to 0.0159. Band 5 shows the largest RMSE, which is consistent with the relatively high sensitivity of NIR reflectance to vegetation condition and surface-moisture variation.

For normalized difference vegetation index (NDVI), the LAPAC and LaSRC kernel density distributions remain broadly consistent, with $R^2 = 0.973$, bias = 0.0032, and RMSE = 0.0479. However, the distributional differences are more evident than those observed for individual reflectance bands, particularly around the intermediate and high NDVI modes. This result is expected because NDVI is a nonlinear transformation of red and NIR reflectance, and residual differences in these

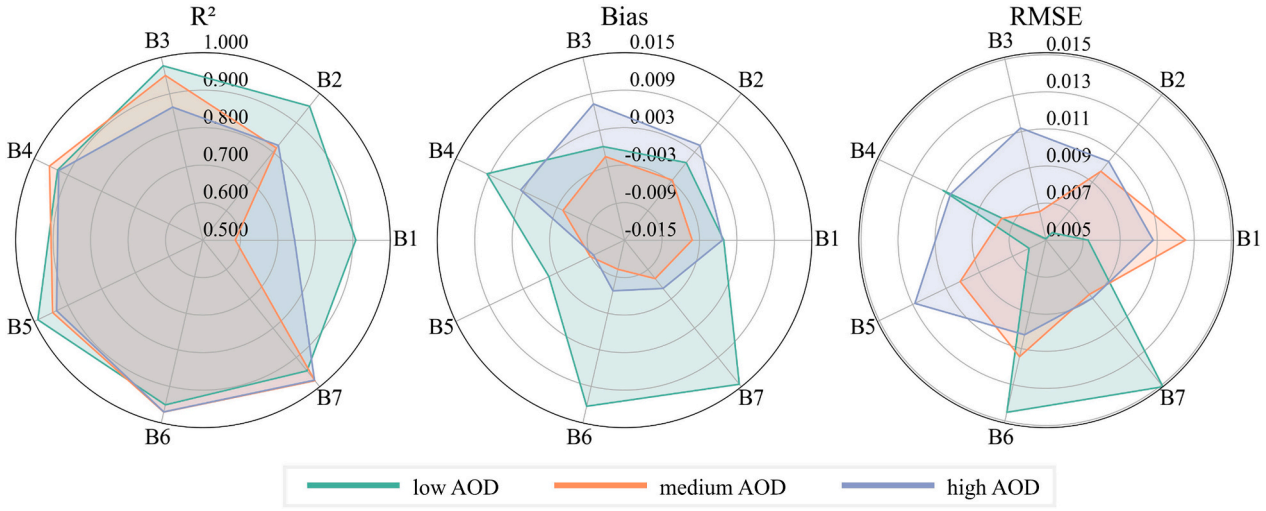


Fig. 12. Radar charts of R^2, bias, and RMSE for Bands 1–7 of Landsat 8 OLI scenes acquired on 16 April 2015, 4 March 2017, and 13 April 2014 under low-, medium-, and high-AOD conditions, respectively, relative to LaSRC surface reflectance. Radial axes represent metric values, and angular axes represent spectral bands.

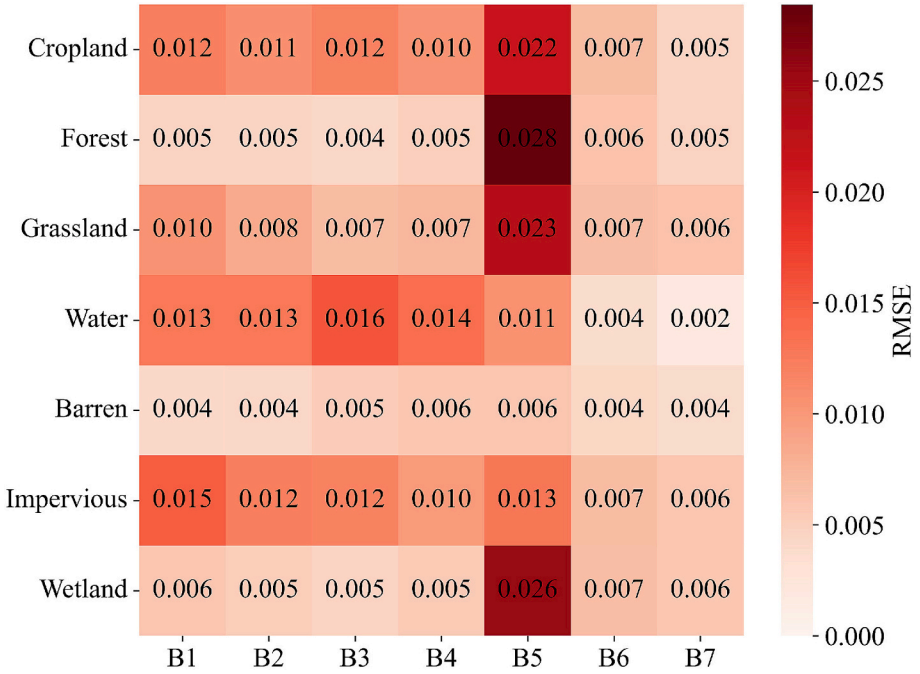


Fig. 13. RMSE heatmap for Bands 1–7 of Landsat 8 OLI scenes acquired on 26 August 2016 over path/row 121/025, 25 July 2016 over path/row 121/036, and 26 July 2016 over path/row 144/033, relative to LaSRC surface reflectance across different land-cover conditions. The horizontal axis represents Landsat 8 bands (B1 to B7), while the vertical axis lists different land cover classes (excluding clouds, cloud shadows, snow/ice, and background). Each cell indicates the RMSE value for the corresponding band and land cover type.

bands can be amplified during index calculation.

3.4. Validation of SR against ground-based measurements

Fig. 15 shows scatter plots comparing satellite-derived surface reflectance with in situ measurements across four validation sites (BSCN, GONA, LCFR, and RVUS). The left column shows results from the proposed method (LAPAC), whereas the right column shows results from the USGS Level-2 product. For LAPAC, R^2 exceeds 0.9 at BSCN (0.943), GONA (0.985), and LCFR (0.969), and is lower at RVUS (0.832). Corresponding RMSE ranges from 0.014 (GONA) to 0.03 (RVUS), with bias remaining near zero at all sites. The Level-2 product shows comparable performance, with R^2 of 0.964 (BSCN), 0.988 (GONA), 0.978 (LCFR), and 0.894 (RVUS), RMSE ranging from 0.012 to 0.024, and bias between −0.007 and 0.007. For LAPAC, the fraction of points within the tolerance envelope $\pm$ (0.05ρ + 0.005) is 56.0% (BSCN), 56.1% (RVUS), 60.2% (LCFR), and 84.9% (GONA), yielding an overall coverage of 66.1%.

LAPAC shows modestly lower stability than the Level-2 product, which is consistent with its reliance on historical Level-2 records as the reference and, consequently, partial dependence on the quality of the official product. Overall, these results indicate that LAPAC retrieves surface reflectance with accuracy close to that of the operational Level-2 product, while residual stability differences likely reflect limitations in the reference data. Although LAPAC does not outperform the operational LaSRC product in this validation, it achieves surface-reflectance accuracy of the same order of magnitude while reducing reliance on contemporaneous external atmospheric ancillary data and a full operational radiative-transfer retrieval workflow.

3.5. Feasibility assessment of Landsat 8-derived PIFs for Landsat 7 correction

Fig. 16 shows the residuals between Landsat 7 surface reflectance and the corresponding in situ measurements (Table 2). The Landsat 7 surface reflectance includes three versions: the official LEDAPS product and two outputs from LAPAC, which use historical reference data from Landsat 7 (Result 1) and Landsat 8 (Result 2), respectively. The kernel density distributions of the residuals (Image − Site) are centered near zero for all three methods, indicating minimal systematic bias. LEDAPS exhibits a narrow, sharply peaked distribution (R^2 = 0.963, bias = 0.002, and RMSE = 0.021), demonstrating strong agreement with the in situ observations. Notably, Result 2 yields an equally concentrated residual distribution and nearly identical errors (R^2 = 0.965, bias = −0.008, RMSE = 0.021), demonstrating LAPAC can reach an absolute accuracy comparable to the official LEDAPS product. In contrast, Result 1 produces a broader residual distribution and markedly worse performance (R^2 = 0.867, bias = 0.003, RMSE = 0.0340), indicating higher random error.

Table 3 compares the cross-sensor consistency between three Landsat 7 surface reflectance products and the temporally nearest, band-transformed Landsat 8 surface reflectance. At the aggregated level (Total), Result 2 shows the most favorable agreement with Landsat 8, achieving the highest R^2 (0.959) and the lowest RMSE (0.025). Relative to LEDAPS, Result 2 reduces the absolute bias from 0.006 to 0.002 (|bias|), indicating improved cross-sensor consistency with a smaller systematic offset while slightly decreasing overall error dispersion (RMSE: 0.027 → 0.025). Consistent with the large sample size ($N = 6.72 \times 10^6$), one-sample tests confirm that the mean biases for all methods and bands are statistically different from zero ($p < 0.05$), with narrow 95% confidence intervals.

- One-sample *t*-tests indicate that the mean bias is significantly different from zero for all bands and for the total statistics ($p < 0.05$; 95% CIs shown in Table A1).
- Paired tests on absolute errors show that Result 2 yields significantly smaller absolute errors than LEDAPS and Result 1 ($p < 0.05$; Cohen's d = −0.196 and − 0.245, respectively).

Band-wise results corroborate this trend. Result 2 generally yields higher R^2 and lower RMSE than LEDAPS and Result 1 across the visible and SWIR bands, with particularly clear improvements in Bands 1–3 and

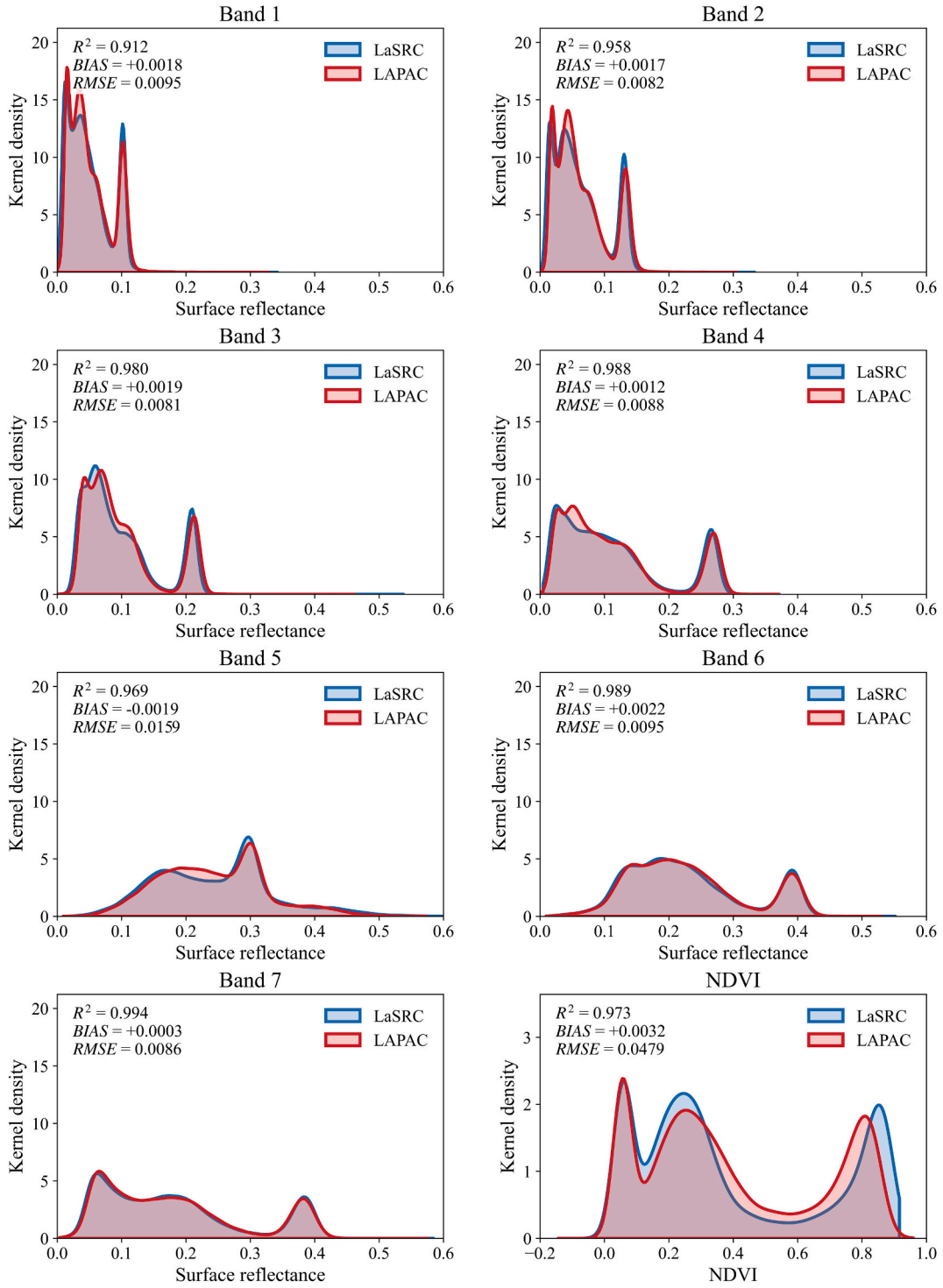


Fig. 14. Band-wise kernel density distributions of LAPAC and LaSRC surface reflectance, aggregated across all study scenes in Table 1. Panels show Landsat 8 OLI Bands 1–7 and NDVI derived from Bands 4 and 5. The distributions were calculated using Gaussian kernel density estimation and normalized to unit area. Kernel density denotes probability density rather than pixel frequency and has reciprocal units of the horizontal-axis variable. Because surface reflectance and NDVI are dimensionless, it is effectively dimensionless. The statistics in the upper-left corner of each panel are R^2, bias, and RMSE, calculated with LaSRC as the designated reference and LAPAC as the compared product.

Band 7. In contrast, Result 1 exhibits weaker overall consistency (R^2 = 0.933) and higher RMSE (0.032), suggesting that the attainable accuracy of LAPAC is sensitive to the quality of the reference reflectance used to construct the constraints. Furthermore, paired tests on absolute errors indicate that Result 2 provides a statistically robust reduction in absolute error compared with LEDAPS and Result 1 ($p < 0.05$; Cohen's d = −0.196 and −0.245, respectively). Collectively, these results support the transferability of Landsat 8–derived reference reflectance (and associated PIF constraints) to Landsat 7 for cross-sensor harmonization, and indicate that using Landsat 8 as the reference yields more consistent cross-sensor agreement for this dataset.

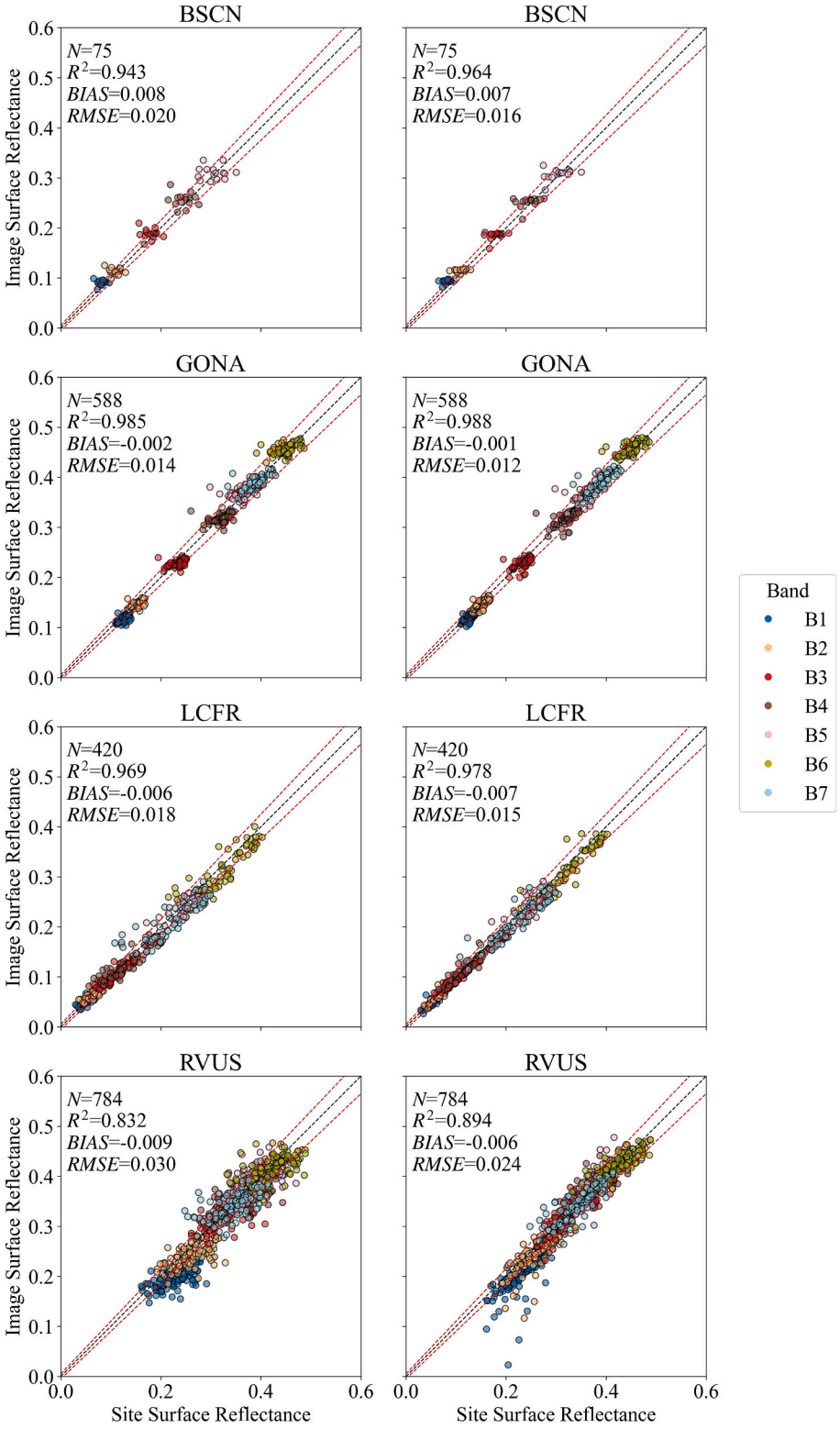


Fig. 15. Scatter plots comparing surface reflectance from LAPAC (left column) and the official Landsat 8 Level-2 product (right column) with site-measured surface reflectance across four validation sites (BSCN, GONA, LCFR, and RVUS). Each point represents observations from Landsat 8 spectral bands (B1–B7). The black dashed line denotes the 1:1 reference line (perfect agreement), and the red dashed lines indicate the surface reflectance specification ($0.05\rho + 0.005$). (For interpretation of the references to colour in this figure legend, the reader is referred to the web version of this article.)

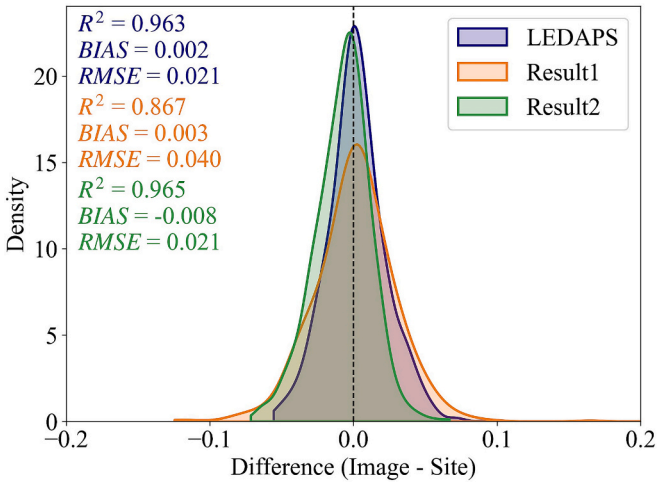


Fig. 16. Kernel density distributions of the differences between Landsat 7 surface reflectance and site-measured surface reflectance for the three retrieval methods. The Landsat 7 surface reflectance was obtained from the official LEDAPS product (LEDAPS), LAPAC using the official Landsat 7 surface reflectance as reference (Result 1), and LAPAC using the official Landsat 8 surface reflectance as reference (Result 2). The vertical dashed line indicates zero bias. The statistical metrics are reported for each method and computed against the site measurements.

4. Discussion

4.1. Influence of land-cover change, cloud contamination, sensor radiometric behavior, and imaging geometry on atmospheric-correction accuracy

LAPAC performs atmospheric correction using PIFs, and its accuracy is influenced by multiple factors, including land-cover changes, cloud contamination, sensor radiometric behavior, and imaging geometry. Surface-condition changes associated with seasonal vegetation phenology, urban expansion, crop rotation, and short-term disturbances can introduce spectral variability even when no permanent land-cover transition occurs (Yan et al., 2019; Zhang et al., 2014; Nguyen and Henebry, 2019), thereby weakening the temporal stability assumption underlying the reference surface reflectance. When the surface state of the reference sequence differs substantially from that of the target acquisition, the inferred atmospheric correction parameters may become biased. This effect is particularly pronounced in regions with rapid vegetation growth, where NIR and SWIR reflectance can vary markedly over short timescales (Nallapareddy, 2022; Shang et al., 2014), potentially contributing to the relatively larger LAPAC–LaSRC discrepancies observed in the SWIR bands in Fig. 12. The relatively larger Band 5 RMSE values for vegetated classes in Fig. 13 are consistent with this potential source of uncertainty, although they cannot by themselves distinguish phenological variation from residual atmospheric-correction error or imperfect reference representativeness.

To mitigate cloud and shadow impacts, we construct the reference surface reflectance from multi-temporal imagery with cloud masking applied and further remove outliers using a *Z*-score filter (Fig. 6). Nevertheless, scenes with high cloud coverage remain challenging to correct reliably. Imperfect cloud masking (Lebreton et al., 2016; Sinabutar et al., 2020; Sun et al., 2019) may leave residual cloud- or shadow-contaminated pixels, producing anomalous TOA reflectance. In addition, a high fraction of invalid pixels within the spatial window reduces the effective sample size and degrades sample quality, which can prevent the correction from meeting the desired error tolerance.

Sensor-related effects also contribute to residual errors. Radiometric performance can degrade over time (Kim et al., 2014; Wang et al., 2024), and orbit drift or long-term changes in imaging geometry can introduce TOA reflectance inconsistencies across acquisition dates (Pinzón et al., 2013; Zhang and Roy, 2016). Because LAPAC is constrained by the long-term stability of PIF-based reference reflectance, it can be more tolerant of moderate TOA perturbations than purely physics-based approaches that require accurate instantaneous atmospheric inputs (Mishra et al., 2016). Moreover, by selecting temporally stable samples and using radiative transfer simulations that span the feasible range of viewing geometries, the method reduces sensitivity to view-angle effects and terrain-induced variability.

4.2. Potential for cross-sensor extension and future work

The site-based validation in Section 3.5 indicates that PIFs extracted from Landsat 8 surface reflectance are transferable to Landsat 7 atmospheric correction. Using Landsat 8 as the reference (Result 2) generally outperforms the Landsat 7–referenced configuration (Result 1), underscoring the benefit of leveraging a higher-quality reference dataset. Relative to LEDAPS, Result 2 reduces the overall bias magnitude from 0.006 to 0.002 (Table 3), supporting the use of PIF-derived constraints as a stable radiometric anchor for cross-sensor harmonization, consistent with prior studies (Fajardo Rueda et al., 2024; Khakurel et al., 2021; Raut et al., 2019; Tuli et al., 2019).

A key advantage of transferable PIF constraints is the suppression of systematic inter-mission offsets arising from sensor-specific processing pipelines and auxiliary inputs (Che et al., 2021). In this study, bias reduction achieved by Result 2 is accompanied by improved dispersion metrics: band-wise statistics generally show higher R^2 and lower RMSE than LEDAPS, and paired tests on absolute errors indicate consistently lower errors for Result 2 relative to both LEDAPS and Result 1 (Table 3). Anchoring the inversion to a more stable reference reflectance therefore improves inter-mission alignment, which is critical for long time series where small persistent offsets can accumulate into spurious trends (Maraun, 2016; Mélin, 2016; Moreno-Martínez et al., 2020).

Several limitations warrant consideration. Our evaluation was restricted to site-centered subsets with relatively homogeneous land cover, so performance over more heterogeneous landscapes remains to

Table 3
Comparison of Landsat 7 surface reflectance with temporally nearest Landsat 8 surface reflectance (Table 2). The Landsat 7 surface reflectance was obtained using three methods: the official LEDAPS product (LEDAPS), LAPAC using the official Landsat 7 surface reflectance as reference (Result 1), and LAPAC using the official Landsat 8 surface reflectance as reference (Result 2). Bias is computed as (Landsat 7 − Landsat 8*), where Landsat 8* denotes the band-transformed Landsat 8 surface reflectance.

Band	LEDAPS			Result 1			Result 2		
	bias	RMSE	R^2	bias	RMSE	R^2	bias	RMSE	R^2
1	0.006	0.023	0.924	0.009	0.032	0.854	−0.001	0.021	0.938
2	0.006	0.022	0.949	0.008	0.03	0.907	−0.001	0.021	0.957
3	0.006	0.025	0.95	0.008	0.032	0.919	−0.003	0.023	0.958
4	−0.002	0.027	0.899	0	0.031	0.87	−0.001	0.027	0.903
5	0.006	0.03	0.918	0.001	0.032	0.905	−0.006	0.029	0.923
7	0.016	0.034	0.905	0.011	0.033	0.909	0.001	0.028	0.934
Total	0.006	0.027	0.951	0.006	0.032	0.933	−0.002	0.025	0.959

be assessed. Future work should expand validation across broader surface types and conditions, and adopt scene-level or block-bootstrap evaluation to account for spatial dependence and quantify uncertainty more realistically. Beyond Landsat, extension to other sensors is promising but requires explicit treatment of cross-sensor differences that affect both PIF selection and the correction mapping, including (i) spectral adjustment for spectral response function mismatches (Chastain et al., 2019; Runge and Grosse, 2019; Scheffler et al., 2020), (ii) incorporation of viewing geometry and bidirectional reflectance distribution function effects (Carmon et al., 2022; Ma et al., 2026; Vögtli et al., 2024), (iii) resolution-aware strategies to mitigate mixed-pixel and adjacency effects (Wang et al., 2021), and (iv) uncertainty-aware weighting that accounts for sensor-specific radiometric stability and noise. These directions provide a testable pathway toward broader multi-mission harmonization with interpretable error sources and uncertainty bounds.

5. Conclusion

This study systematically constructs a long-term stable PIF set from the Landsat surface reflectance archive, providing an independent reference for atmospheric correction. By leveraging archive-derived stability constraints based on PIFs, LAPAC removes the reliance on concurrent external atmospheric data, which can improve the timeliness in operational atmospheric correction and cross-mission consistency in surface reflectance products. Compared with the existing aerosol-retrieval schemes that depend on suitable low-reflectance targets and surface-type assumptions, LAPAC automatically selects sufficient PIFs by ranking within-scene pixels using relative stability metrics and then uses simple radiative transfer simulations matched with the satellite observations to initialize and optimize the iterative inversion of surface and atmospheric variables. Together, these improve the algorithm robustness, enabling broad applicability across land-cover conditions and scalability to the full Landsat archive.

Compared with the official LaSRC product, LAPAC achieved consistently good agreement on surface reflectance across varying AOD regimes and land-cover types, yielding a mean R^2 of 0.91 for Bands 1–7, with $|\text{bias}| \leq 0.015$ and RMSE $\leq$0.015 across all AOD conditions, while RMSE across most land-cover classes remained within 0.004–0.016. At RadCalNet stations (BSCN, GONA, LCFR, and RVUS), the method shows strong agreement with in situ measurements ($R^2 \geq 0.832$), with RMSE reaching as low as 0.014 at multiple locations.

Using Landsat 8 surface reflectance as a high-quality reference, LAPAC further suppresses systematic biases in Landsat 7 atmospheric correction, achieving $|\text{bias}| = 0.002$ (versus 0.006 for LEDAPS), RMSE $= 0.025$, and strong cross-mission consistency ($R^2 = 0.959$).

However, performance remains sensitive to the quality of the PIF pixel set. With heavy cloud contamination or substantial land-surface change, the archive-based reference may become unreliable. In addition, errors may propagate more strongly over densely vegetated areas (e.g., in NIR Band 5) and into index-based products such as NDVI. Further optimization is needed to strengthen error control and improve model generalization.

Overall, this study advances a practical paradigm for atmospheric correction by leveraging historical observations and integrating data-driven constraints with physical modeling to establish a near real time, high-accuracy, cross-generational, and input-independent atmospheric correction framework. LAPAC shows strong potential for achieving continuous long-term Earth observations, consistency cross-sensor time series analysis, and accurate downstream applications such as surface parameter retrievals.

CRediT authorship contribution statement

Wenchang Li: Writing – original draft, Visualization, Validation, Software, Methodology, Investigation, Formal analysis, Data curation. **Tao He:** Conceptualization, Methodology, Formal analysis, Writing – review & editing, Supervision, Resources, Funding acquisition.

Code availability

The program developed and used in this study is publicly available at Zenodo: https://doi.org/10.5281/zenodo.17695622.

Declaration of competing interest

The authors declare that they have no known competing financial interests or personal relationships that could have appeared to influence the work reported in this paper.

Acknowledgments

The authors gratefully acknowledge the journal's editorial team and the anonymous reviewers for their constructive and insightful comments, which substantially improved this manuscript and the research. This research was supported by the National Key Research and Development Project of China (grant no. 2025YFE0211500), the National Natural Science Foundation of China (General Program) (grant no. 42571425) and the Anhui Province Natural Resources Science and Technology Project (2025-K-4).

Appendix A

Table A1
Sample size (N), mean bias, and 95% confidence interval (CI) of the bias for each Landsat 7 surface reflectance product relative to the temporally nearest, band-transformed Landsat 8 surface reflectance.

Band	N	95% CI		
		LEDAPS	Result1	Result2
1	1,120,000	[0.0055, 0.0056]	[0.0087, 0.0088]	[−0.0006, −0.0005]
2	1,120,000	[0.0057, 0.0058]	[0.0080, 0.0081]	[−0.0012, −0.0011]
3	1,120,000	[0.0064, 0.0065]	[0.0082, 0.0083]	[−0.0031, −0.0030]
4	1,120,000	[−0.0018, −0.0017]	[0.0001, 0.0002]	[−0.0012, −0.0011]
5	1,120,000	[0.0058, 0.0059]	[0.0010, 0.0012]	[−0.0061, −0.0060]
7	1,120,000	[0.0160, 0.0161]	[0.0114, 0.0115]	[0.0011, 0.0012]
Total	6,720,000	[0.0063, 0.0064]	[0.0062, 0.0063]	[−0.0018, −0.0018]

Data availability

Data will be made available on request.

References

Bouvet, M., Thome, K., Berthelot, B., Bialek, A., Czapla-Myers, J., Fox, N.P., Goryl, P., Henry, P., Ma, L., Marcq, S., Meygret, A., Wenny, B.N., Woolliams, E.R., 2019. RadCalNet: a radiometric calibration network for earth observing imagers operating in the visible to shortwave infrared spectral range. Remote Sens. 11, 2401. https://doi.org/10.3390/rs11202401.

Carmon, N., Berk, A., Bohn, N., Brodrick, P.G., Kalashnikova, O., Nguyen, H., Thompson, D.R., Turmon, M., 2022. Unified topographic and atmospheric correction for remote imaging spectroscopy. Front. Remote Sens. 3. https://doi.org/10.3389/frsen.2022.916155.

Chastain, R., Housman, I., Goldstein, J., Finco, M., Tenneson, K., 2019. Empirical cross sensor comparison of sentinel-2A and 2B MSI, landsat-8 OLI, and landsat-7 ETM+ top of atmosphere spectral characteristics over the conterminous United States. Remote Sens. Environ. 221, 274–285.

Che, X., Zhang, H.K., Liu, J., 2021. Making Landsat 5, 7 and 8 reflectance consistent using MODIS nadir-BRDF adjusted reflectance as reference. Remote Sens. Environ. 262, 112517. https://doi.org/10.1016/j.rse.2021.112517.

Chen, L., Ma, Y., Lian, Y., Zhang, H., Yu, Y., Lin, Y., 2023. Radiometric normalization using a Pseudo−invariant polygon features−based algorithm with contemporaneous sentinel−2A and Landsat−8 OLI imagery. Appl. Sci. 13, 2525. https://doi.org/10.3390/app13042525.

Chen, L., Wang, R., Fei, Y., Fang, P., Zha, Y., Chen, H., 2024. Multi-angle aerosol optical depth retrieval method based on improved surface reflectance. Atmos. Meas. Tech. 17, 4411–4424. https://doi.org/10.5194/amt-17-4411-2024.

Cheng, J., Meng, X., Dong, S., Liang, S., 2021. Generating the 30-m land surface temperature product over continental China and USA from landsat 5/7/8 data. Sci. Remote Sens. 4, 100032. https://doi.org/10.1016/j.srs.2021.100032.

Chi, Y., Wu, Z., Liao, K., Ren, Y., 2020. Handling missing data in large-scale MODIS AOD products using a two-step model. Remote Sens. 12, 3786. https://doi.org/10.3390/rs12223786.

Chikodili, N.B., Abdulmalik, M.D., Abisoye, O.A., Bashir, S.A., 2021. Outlier detection in multivariate time series data using a fusion of K-medoid, standardized Euclidean distance and Z-score. In: Misra, S., Muhammad-Bello, B. (Eds.), Information and Communication Technology and Applications. Springer International Publishing, Cham, pp. 259–271. https://doi.org/10.1007/978-3-030-69143-1_21.

Claverie, M., Ju, J., Masek, J.G., Dungan, J.L., Vermote, E.F., Roger, J.-C., Skakun, S.V., Justice, C., 2018. The harmonized Landsat and Sentinel-2 surface reflectance data set. Remote Sens. Environ. 219, 145–161. https://doi.org/10.1016/j.rse.2018.09.002.

Coleman, R.W., Thompson, D.R., Brodrick, P.G., Dor, E.B., Cox, E., Pérez García-Pando, C., Hoefen, T., Kokaly, R.F., Meyer, J.M., Ochoa, F., Okin, G.S., Pearlshtien, D.H., Swayze, G., Green, R.O., 2024. An accuracy assessment of the surface reflectance product from the EMIT imaging spectrometer. Remote Sens. Environ. 315, 114450. https://doi.org/10.1016/j.rse.2024.114450.

Crawford, C.J., Roy, D.P., Arab, S., Barnes, C., Vermote, E., Hulley, G., Gerace, A., Choate, M., Engebretson, C., Micijevic, E., Schmidt, G., Anderson, C., Anderson, M., Bouchard, M., Cook, B., Dittmeier, R., Howard, D., Jenkerson, C., Kim, M., Kleyians, T., Maiersperger, T., Mueller, C., Neigh, C., Owen, L., Page, B., Pahlevan, N., Rengarajan, R., Roger, J.-C., Sayler, K., Scaramuzza, P., Skakun, S., Yan, L., Zhang, H.K., Zhu, Z., Zahn, S., 2023. The 50-year Landsat collection 2 archive. Sci. Remote Sens. 8, 100103. https://doi.org/10.1016/j.srs.2023.100103.

Denaro, L.G., Lin, C.-H., 2020. Hybrid canonical correlation analysis and regression for radiometric normalization of cross-sensor satellite imagery. IEEE J. Sel. Top. Appl. Earth Obs. Remote Sens. 13, 976–986.

Doxani, G., Vermote, E.F., Roger, J.-C., Skakun, S., Gascon, F., Collison, A., De Keukelaere, L., Desjardins, C., Frantz, D., Hagolle, O., Kim, M., Louis, J., Pacifici, F., Pflug, B., Poilvé, H., Ramon, D., Richter, R., Yin, F., 2023. Atmospheric correction inter-comparison eXercise, ACIX-II land: an assessment of atmospheric correction processors for Landsat 8 and Sentinel-2 over land. Remote Sens. Environ. 285, 113412. https://doi.org/10.1016/j.rse.2022.113412.

Emde, C., Buras-Schnell, R., Kylling, A., Mayer, B., Gasteiger, J., Hamann, U., Kylling, J., Richter, B., Pause, C., Dowling, T., et al., 2016. The libRadtran software package for radiative transfer calculations (version 2.0. 1). Geosci. Model Dev. 9, 1647–1672.

Ettehadi Osgouei, P., Roberts, G., Kaya, S., Bilal, M., Dash, J., Sertel, E., 2022. Evaluation and comparison of MODIS and VIIRS aerosol optical depth (AOD) products over regions in the eastern Mediterranean and the Black Sea. Atmos. Environ. 268, 118784. https://doi.org/10.1016/j.atmosenv.2021.118784.

Fajardo Rueda, J., Leigh, L., Pinto, C.T., 2024. A global mosaic of temporally stable pixels for radiometric calibration of optical satellite sensors using Landsat 8. Remote Sens. 16, 2437. https://doi.org/10.3390/rs16132437.

Flood, N., 2017. Comparing sentinel-2A and Landsat 7 and 8 using surface reflectance over Australia. Remote Sens. 9, 659. https://doi.org/10.3390/rs9070659.

Foga, S., Scaramuzza, P.L., Guo, S., Zhu, Z., Dilley, R.D., Beckmann, T., Schmidt, G.L., Dwyer, J.L., Joseph Hughes, M., Laue, B., 2017. Cloud detection algorithm comparison and validation for operational Landsat data products. Remote Sens. Environ. 194, 379–390. https://doi.org/10.1016/j.rse.2017.03.026.

Frantz, D., Stellmes, M., Hostert, P., 2019. A global MODIS water vapor database for the operational atmospheric correction of historic and recent Landsat imagery. Remote Sens. 11, 257. https://doi.org/10.3390/rs11030257.

Groeneveld, D.P., Ruggles, T.A., 2023. An algorithm developed for Smallsats accurately retrieves Landsat surface reflectance using scene statistics. Appl. Sci. 13, 12604. https://doi.org/10.3390/app132312604.

Groeneveld, D.P., Ruggles, T.A., Gao, B.-C., 2023. Closed-form method for atmospheric correction (CMAC) of Smallsat data using scene statistics. Appl. Sci. 13, 6352. https://doi.org/10.3390/app13106352.

Hall, F.G., Strebel, D.E., Nickeson, J.E., Goetz, S.J., 1991. Radiometric rectification: toward a common radiometric response among multidate, multisensor images. Remote Sens. Environ. 35, 11–27.

He, T., Liang, S., Wang, D., Chen, X., Song, D.-X., Jiang, B., 2015. Land surface albedo estimation from Chinese HJ satellite data based on the direct estimation approach. Remote Sens. 7, 5495–5510. https://doi.org/10.3390/rs70505495.

He, T., Liang, S., Wang, D., Cao, Y., Gao, F., Yu, Y., Feng, M., 2018. Evaluating land surface albedo estimation from Landsat MSS, TM, ETM +, and OLI data based on the unified direct estimation approach. Remote Sens. Environ. 204, 181–196. https://doi.org/10.1016/j.rse.2017.10.031.

Hsu, N.C., Tsay, S.-C., King, M.D., Herman, J.R., 2004. Aerosol properties over bright-reflecting source regions. IEEE Trans. Geosci. Remote Sens. 42, 557–569. https://doi.org/10.1109/TGRS.2004.824067.

Hsu, N.C., Tsay, S.-C., King, M.D., Herman, J.R., 2006. Deep blue retrievals of Asian aerosol properties during ACE-Asia. IEEE Trans. Geosci. Remote Sens. 44, 3180–3195. https://doi.org/10.1109/TGRS.2006.879540.

Hsu, N.C., Jeong, M.-J., Bettenhausen, C., Sayer, A.M., Hansell, R., Seftor, C.S., Huang, J., Tsay, S.-C., 2013. Enhanced deep blue aerosol retrieval algorithm: the second generation. J. Geophys. Res. Atmos. 118, 9296–9315. https://doi.org/10.1002/jgrd.50712.

Ientilucci, E.J., Adler-Golden, S., 2019. Atmospheric compensation of hyperspectral data: an overview and review of in-scene and physics-based approaches. IEEE Geosci. Remote Sens. Mag. 7, 31–50. https://doi.org/10.1109/MGRS.2019.2904706.

Jin, H., Li, A., Xu, W., Xiao, Z., Jiang, J., Xue, H., 2019. Evaluation of topographic effects on multiscale leaf area index estimation using remotely sensed observations from multiple sensors. ISPRS J. Photogramm. Remote Sens. 154, 176–188. https://doi.org/10.1016/j.isprsjprs.2019.06.008.

Kaufman, Y.J., Remer, L.A., 1994. Detection of forests using mid-IR reflectance: an application for aerosol studies. IEEE Trans. Geosci. Remote Sens. 32, 672–683. https://doi.org/10.1109/36.297984.

Khakurel, P., Leigh, L., Kaewmanee, M., Pinto, C.T., 2021. Extended Pseudo invariant calibration site-based trend-to-trend cross-calibration of optical satellite sensors. Remote Sens. 13, 1545. https://doi.org/10.3390/rs13081545.

Kim, T., Han, Y., 2021. Integrated Preprocessing of multitemporal very-high-resolution satellite images via conjugate points-based Pseudo-invariant feature extraction. Remote Sens. 13, 3990. https://doi.org/10.3390/rs13193990.

Kim, W., He, T., Wang, D., Cao, C., Liang, S., 2014. Assessment of long-term sensor radiometric degradation using time series analysis. IEEE Trans. Geosci. Remote Sens. 52, 2960–2976. https://doi.org/10.1109/TGRS.2013.2268161.

Kotchenova, S.Y., Vermote, E.F., 2007. Validation of a vector version of the 6S radiative transfer code for atmospheric correction of satellite data. Part II. Homogeneous Lambertian and anisotropic surfaces. Appl. Optics 46, 4455–4464. https://doi.org/10.1364/AO.46.004455.

Kotchenova, S.Y., Vermote, E.F., Matarrese, R., Frank, J., Klemm, J., 2006. Validation of a vector version of the 6S radiative transfer code for atmospheric correction of satellite data. Part I: Path radiance. Appl. Opt. 45, 6762–6774. https://doi.org/10.1364/AO.45.006762.

Lebreton, C., Stelzer, K., Brockmann, C., Pringle, N., Paperin, M., Danne, O., Knaeps, E., Ruddick, K., 2016. METH-103-Cloud and Cloud Shadow Masking of High and Medium Resolution Optical Sensors – An Algorithm Inter-Comparison Example for Landsat 8.

Lhissou, R., El Harti, A., Maimouni, S., Adiri, Z., et al., 2020. Assessment of the image-based atmospheric correction of multispectral satellite images for geological mapping in arid and semi-arid regions. Remote Sens. Appl. Soc. Environ. 20, 100420.

Li, C., Ma, L., Gao, C., Tang, L., Wang, N., Liu, Y., Zhao, Y., Dou, S., Zhang, D., Li, X., 2015. Permanent target for optical payload performance and data quality assessment: spectral characterization and a case study for calibration. J. Appl. Remote. Sens. 8, 083498. https://doi.org/10.1117/1.JRS.8.083498.

Li, J., Xiao, Z., Sun, R., Song, J., 2023. A method to estimate leaf area index from VIIRS surface reflectance using deep transfer learning. ISPRS J. Photogramm. Remote Sens. 202, 512–527. https://doi.org/10.1016/j.isprsjprs.2023.07.012.

Lin, B.-Y., Wang, Z.-J., Syariz, M.A., Denaro, L.G., Lin, C.-H., 2019. Pseudoinvariant feature selection using multitemporal MAD for optical satellite images. IEEE Geosci. Remote Sens. Lett. 16, 1353–1357.

Lubke, M., Rengarajan, R., Choate, M., 2021. Preliminary Assessment of the Geometric Improvements to the Landsat Collection-2 Archive, in: Earth Observing Systems XXVI. Presented at the Earth Observing Systems XXVI. SPIE, pp. 125–137. https://doi.org/10.1117/12.2596200.

Lyapustin, A., Wang, Y., 2022. MODIS/Terra+aqua land aerosol optical depth daily L2G global 1km SIN grid V061. NASA EOSDIS land process. In: Distrib. Act. Arch. Cent. DAAC Data Set MCD19A2.061. https://doi.org/10.5067/MODIS/MCD19A2.061.

Ma, L., Zhao, Y., Woolliams, E.R., Dai, C., Wang, N., Liu, Y., Li, L., Wang, X., Gao, C., Li, C., Tang, L., 2020. Uncertainty analysis for RadCalNet instrumented test sites using the Baotou sites BTCN and BSCN as examples. Remote Sens. 12, 1696. https://doi.org/10.3390/rs12111696.

Ma, Y., Liang, S., Ma, H., He, T., Shi, X., Li, W., Cai, D., Xiao, X., Guan, S., Liu, W., Xu, J., Chen, Y., Zhang, Y., 2026. An integrated atmospheric-topographic correction framework for land surface reflectance estimation using a spatial-spectral attention

U-net model. Remote Sens. Environ. 334, 115188. https://doi.org/10.1016/j.rse.2025.115188.
Maraun, D., 2016. Bias correcting climate change simulations - a critical review. Curr. Clim. Change Rep. 2, 211–220. https://doi.org/10.1007/s40641-016-0050-x.
Masek, J.G., Vermote, E.F., Saleous, N.E., Wolfe, R., Hall, F.G., Huemmrich, K.F., Gao, F., Kutler, J., Lim, T.K., 2006. A landsat surface reflectance dataset for North America, 1990-2000. IEEE Geosci. Remote Sens. Lett. 3, 68–72. https://doi.org/10.1109/LGRS.2005.857030.
Masek, J.G., Vermote, E.F., Saleous, N., Wolfe, R., Hall, F.G., Huemmrich, K.F., Gao, F., Kutler, J., Lim, T.K., 2012. LEDAPS Landsat Calibration, Reflectance, Atmospheric Correction Preprocessing Code. ORNL DAAC. https://doi.org/10.3334/ORNLDAAC/1080.
Masek, J.G., Vermote, E.F., Saleous, N., Wolfe, R., Hall, F.G., Huemmrich, K.F., Gao, F., Kutler, J., Lim, T.K., 2013. LEDAPS calibration, reflectance, atmospheric correction preprocessing code, version 2. ORNL DAAC. https://doi.org/10.3334/ORNLDAAC/1146.
Mélin, F., 2016. Impact of inter-mission differences and drifts on chlorophyll-a trend estimates. Int. J. Remote Sens. 37, 2233–2251. https://doi.org/10.1080/01431161.2016.1168949.
Mishra, N., Helder, D., Barsi, J., Markham, B., 2016. Continuous calibration improvement in solar reflective bands: Landsat 5 through Landsat 8. Remote Sens. Environ., Landsat 8 Science Results 185, 7–15. https://doi.org/10.1016/j.rse.2016.07.032.
Moreno-Martínez, Á., Izquierdo-Verdiguier, E., Maneta, M.P., Camps-Valls, G., Robinson, N., Muñoz-Marí, J., Sedano, F., Clinton, N., Running, S.W., 2020. Multispectral high resolution sensor fusion for smoothing and gap-filling in the cloud. Remote Sens. Environ. 247, 111901. https://doi.org/10.1016/j.rse.2020.111901.
Nallapareddy, A., 2022. Detection and classification of vegetation areas from red and near infrared bands of LANDSAT-8 optical satellite image. Appl. Comput. Sci. 18. https://doi.org/10.35784/acs-2022-4.
Nazeer, M., Ilori, C.O., Bilal, M., Nichol, J.E., Wu, W., Qiu, Z., Gayene, B.K., 2021. Evaluation of atmospheric correction methods for low to high resolutions satellite remote sensing data. Atmos. Res. 249, 105308. https://doi.org/10.1016/j.atmosres.2020.105308.
Neelin, J.D., Martinez-Villalobos, C., Stechmann, S.N., Ahmed, F., Chen, G., Norris, J.M., Kuo, Y.-H., Lenderink, G., 2022. Precipitation extremes and water vapor. Curr. Clim. Chang. Rep. 8, 17–33. https://doi.org/10.1007/s40641-021-00177-z.
Nguyen, L.H., Henebry, G.M., 2019. Characterizing land use/land cover using multi-sensor time series from the perspective of land surface phenology. Remote Sens. 11, 1677. https://doi.org/10.3390/rs11141677.
Pinzón, J.E., Brown, M.E., Tucker, C.J., 2013. Emd correction of orbital drift artifacts in satellite data stream. In: Hilbert?Huang Transform and its Applications, Interdisciplinary Mathematical Sciences. WORLD SCIENTIFIC, pp. 241–260. https://doi.org/10.1142/9789814508247_0011.
Pons, X., Pesquer, L., Cristóbal, J., González-Guerrero, O., 2014. Automatic and improved radiometric correction of Landsat imagery using reference values from MODIS surface reflectance images. Int. J. Appl. Earth Obs. Geoinformation 33, 243–254. https://doi.org/10.1016/j.jag.2014.06.002.
Raut, B., Kaewmanee, M., Angal, A., Xiong, X., Helder, D., 2019. Empirical absolute calibration model for multiple pseudo-invariant calibration sites. Remote Sens. 11, 1105. https://doi.org/10.3390/rs11091105.
Rengarajan, R., Choate, M., Storey, J., Franks, S., Micijevic, E., 2020. Landsat Collection-2 Geometric Calibration Updates, in: Earth Observing Systems XXV. Presented at the Earth Observing Systems XXV. SPIE, pp. 85–95. https://doi.org/10.1117/12.2570429.
Roy, D.P., Qin, Y., Kovalskyy, V., Vermote, E.F., Ju, J., Egorov, A., Hansen, M.C., Kommareddy, I., Yan, L., 2014. Conterminous United States demonstration and characterization of MODIS-based Landsat ETM + atmospheric correction. Remote Sens. Environ. 140, 433–449. https://doi.org/10.1016/j.rse.2013.09.012.
Runge, A., Grosse, G., 2019. Comparing spectral characteristics of Landsat-8 and Sentinel-2 same-day data for Arctic-boreal regions. Remote Sens. 11, 1730. https://doi.org/10.3390/rs11141730.
Scheffler, D., Frantz, D., Segl, K., 2020. Spectral harmonization and red edge prediction of Landsat-8 to Sentinel-2 using land cover optimized multivariate regressors. Remote Sens. Environ. 241, 111723.
Schläpfer, D., Borel, C.C., Keller, J., Itten, K.I., 1998. Atmospheric precorrected differential absorption technique to retrieve columnar water vapor. Remote Sens. Environ. 65, 353–366.
Schott, J.R., Salvaggio, C., Volchok, W.J., 1988. Radiometric scene normalization using pseudoinvariant features. Remote Sens. Environ. 26, 1–16. https://doi.org/10.1016/0034-4257(88)90116-2.
Servera, J.V., Rivera-Caicedo, J.P., Verrelst, J., Muñoz-Marí, J., Sabater, N., Berthelot, B., Camps-Valls, G., Moreno, J., 2021. Systematic assessment of MODTRAN emulators for atmospheric correction. IEEE Trans. Geosci. Remote Sens. 60, 1–17.
Shang, J., Liu, J., Huffman, T., Qian, B., Pattey, E., Wang, J., Zhao, T., Geng, X., Kroetsch, D., Dong, T., Lantz, N., 2014. Estimating plant area index for monitoring crop growth dynamics using Landsat-8 and RapidEye images. J. Appl. Remote Sens. 8, 085196. https://doi.org/10.1117/1.JRS.8.085196.
Sinabutar, J.J., Sasmito, B., Sukmono, A., 2020. STUDI cloud masking MENGGUNAKAN band quality assessment, function of mask dan multi-temporal cloud masking pada CITRA LANDSAT 8. J. Geod. Undip 9, 51–60. https://doi.org/10.14710/jgundip.2020.28123.
Sun, M., Bo, Y., Cui, L., Li, R.Y., 2019. An Improved Fmask Algorithm in Tropical Regions for Landsat Images. IGARSS 2019–2019 IEEE int. Geosci. Remote Sens. Symp, pp. 1562–1565. https://doi.org/10.1109/IGARSS.2019.8899789.
Syariz, M.A., Lin, B.-Y., Denaro, L.G., Jaelani, L.M., Van Nguyen, M., Lin, C.-H., 2019. Spectral-consistent relative radiometric normalization for multitemporal Landsat 8 imagery. ISPRS J. Photogramm. Remote Sens. 147, 56–64. https://doi.org/10.1016/j.isprsjprs.2018.11.007.
Tanre, D., Herman, M., Deschamps, P.Y., De Leffe, A., 1979. Atmospheric modeling for space measurements of ground reflectances, including bidirectional properties. Appl. Optics 18, 3587. https://doi.org/10.1364/AO.18.003587.
Tuli, F.T.Z., Pinto, C.T., Angal, A., Xiong, X., Helder, D., 2019. New approach for temporal stability evaluation of Pseudo-invariant calibration sites (PICS). Remote Sens. 11, 1502. https://doi.org/10.3390/rs11121502.
Vermote, E.F., Tanre, D., Deuze, J.L., Herman, M., Morcrette, J.J., 2006. Second simulation of a satellite signal in the solar spectrum-vector (6SV). IEEE. https://doi.org/10.1109/IGARSS.1990.688308.
Vermote, E., Justice, C., Claverie, M., Franch, B., 2016. Preliminary analysis of the performance of the Landsat 8/OLI land surface reflectance product. Remote Sens. Environ., Landsat 8 Science Results 185, 46–56. https://doi.org/10.1016/j.rse.2016.04.008.
Vögtli, M., Schläpfer, D., Schuman, M.C., Schaepman, M.E., Kneubühler, M., Damm, A., 2024. Effects of atmospheric, topographic, and BRDF correction on imaging spectroscopy-derived data products. IEEE J. Sel. Top. Appl. Earth Obs. Remote Sens. 17, 109–126. https://doi.org/10.1109/JSTARS.2023.3325926.
Wang, T., Du, L., Yi, W., Hong, J., Zhang, L., Zheng, J., Li, C., Ma, X., Zhang, D., Fang, W., Huang, H., Wang, A., Song, B., Zhou, N., Ti, R., Li, K., Cui, W., 2021. An adaptive atmospheric correction algorithm for the effective adjacency effect correction of submeter-scale spatial resolution optical satellite images: application to a WorldView-3 panchromatic image. Remote Sens. Environ. 259, 112412. https://doi.org/10.1016/j.rse.2021.112412.
Wang, J., Hu, X., Wang, L., Zhang, B., Miao, S., 2024. Instrument degradation monitoring with big data analysis of global pseudo-invariant pixels. IGARSS 2024–2024. IEEE Int. Geosci. Remote Sens. Symp. 6197–6200. https://doi.org/10.1109/IGARSS53475.2024.10642758.
Wang, Y., Liu, L., Hu, Y., Li, D., Li, Z., 2016. Development and validation of the Landsat-8 surface reflectance products using a modis-based per-pixel atmospheric correction method. Int. J. Remote Sens. 37, 1291–1314. https://doi.org/10.1080/01431161.2015.1104742.
Xu, H., Wei, Y., Li, X., Zhao, Y., Cheng, Q., 2021. A novel automatic method on pseudo-invariant features extraction for enhancing the relative radiometric normalization of high-resolution images. Int. J. Remote Sens. 42, 6153–6183.
Yan, J., Wang, L., Song, W., Chen, Y., Chen, X., Deng, Z., 2019. A time-series classification approach based on change detection for rapid land cover mapping. ISPRS J. Photogramm. Remote Sens. 158, 249–262. https://doi.org/10.1016/j.isprsjprs.2019.10.003.
Yang, J., Hu, M., 2018. Filling the missing data gaps of daily MODIS AOD using spatiotemporal interpolation. Sci. Total Environ. 633, 677–683. https://doi.org/10.1016/j.scitotenv.2018.03.202.
Yang, J., Huang, X., 2024. The 30 M Annual Land Cover Datasets and its Dynamics in China from 1985 to 2023. https://doi.org/10.5281/zenodo.12779975.
You, W., Zang, Z., Zhang, L., Li, Y., Pan, X., Wang, W., 2016. National-Scale Estimates of ground-level PM2.5 concentration in China using geographically weighted regression based on 3 km resolution MODIS AOD. Remote Sens. 8, 184. https://doi.org/10.3390/rs8030184.
Yu, K., Liu, S., Zhao, Y., 2016. CPBAC: a quick atmospheric correction method using the topographic information. Remote Sens. Environ. 186, 262–274. https://doi.org/10.1016/j.rse.2016.08.010.
Zhang, H.K., Roy, D.P., 2016. Landsat 5 thematic mapper reflectance and NDVI 27-year time series inconsistencies due to satellite orbit change. Remote Sens. Environ. 186, 217–233. https://doi.org/10.1016/j.rse.2016.08.022.
Zhang, P., Lv, Z., Shi, W., 2014. Local Spectrum-trend similarity approach for detecting land-cover change by using SPOT-5 satellite images. IEEE Geosci. Remote Sens. Lett. 11, 738–742. https://doi.org/10.1109/LGRS.2013.2278205.
Zhang, Y., Liang, S., Zhu, Z., Ma, H., He, T., 2022. Soil moisture content retrieval from Landsat 8 data using ensemble learning. ISPRS J. Photogramm. Remote Sens. 185, 32–47. https://doi.org/10.1016/j.isprsjprs.2022.01.005.
Zhou, H., Liu, S., He, J., Wen, Q., Song, L., Ma, Y., 2016. A new model for the automatic relative radiometric normalization of multiple images with pseudo-invariant features. Int. J. Remote Sens. 37, 4554–4573.